

# Code-Verification Techniques for an Arbitrary-Depth Electromagnetic Slot Model

Brian A. Freno<sup>a</sup>, Neil R. Matula<sup>a</sup>, Robert A. Pfeiffer<sup>a</sup>, Vinh Q. Dang<sup>a</sup>

<sup>a</sup>*Sandia National Laboratories, Albuquerque, NM 87185*

---

## Abstract

Electromagnetic penetration through openings in an otherwise closed electromagnetic scatterer is an important topic in computational electromagnetics. To efficiently model this phenomenon, aperture or slot models are often used in conjunction with surface integral equations to solve Maxwell's equations. To establish the credibility of these models, code verification is necessary to assess the correctness of the implementation of the underlying numerical methods. However, many characteristics of surface integral equations and slot models render traditional code-verification approaches ineffective. In this paper, we present approaches to separately measure the different sources of numerical error arising from the method-of-moments implementation of the electric-field integral equation with an arbitrary-depth slot model. We demonstrate the effectiveness of these approaches for several cases.

*Keywords:* electromagnetic penetration, code verification, electric-field integral equation, manufactured solutions, electromagnetic slot models

---

## 1. Introduction

Electromagnetic penetration, which occurs through intentional or inadvertent openings in an otherwise closed electromagnetic scatterer, is an important topic in computational electromagnetics. Practically every material interface presents an opportunity for an intentional or unintentional opening [1]. Through electromagnetic penetration, the exterior and interior electromagnetic fields interact.

To efficiently model this phenomenon, aperture or slot models are often used in conjunction with surface integral equations (SIEs), such as the electric-, magnetic-, and combined-field equations, to solve Maxwell's equations. Rectangular apertures and slots are among the most common antennas in practice [2, Chap. 8].

The width of the slot is typically small compared to the overall size of the scatterer. Hence, while it is possible to explicitly discretize the slot interior as part of the surface of the scatterer, the computational expense needed to resolve the small length scales in the vicinity and interior of the slot may be prohibitive. As an alternative, the slot may be modeled by replacing it with a conceptually simpler geometry, such as a system of conducting wires embedded in the surrounding surface [3]. The development and validation of aperture and slot models remain active research topics [4–13].

Code verification plays a critical role in establishing the credibility of results from computational physics simulations by assessing the correctness of the implementation of the underlying numerical methods [14–16]. The discretization of differential, integral, and integro-differential equations introduces a discretization error in the solution. The correctness of the implementation of the numerical methods can be verified by comparing the rate at which the error decreases as the discretization is refined with the expected rate for numerous test cases. To compute the error, the method of manufactured solutions [17] is a commonly used approach to produce problems of arbitrary complexity with known solutions.

There are numerous examples of code verification in computational mechanics and heat transfer [18–32] and computational electromagnetics and plasma sciences [33–39]. For electromagnetic SIEs, code-verification activities that employ manufactured solutions have been described for the electric-field integral equation (EFIE) [40–44], magnetic-field integral equation [45], and combined-field integral equation [46].

---

*Email address:* bafreno@sandia.gov (Brian A. Freno)

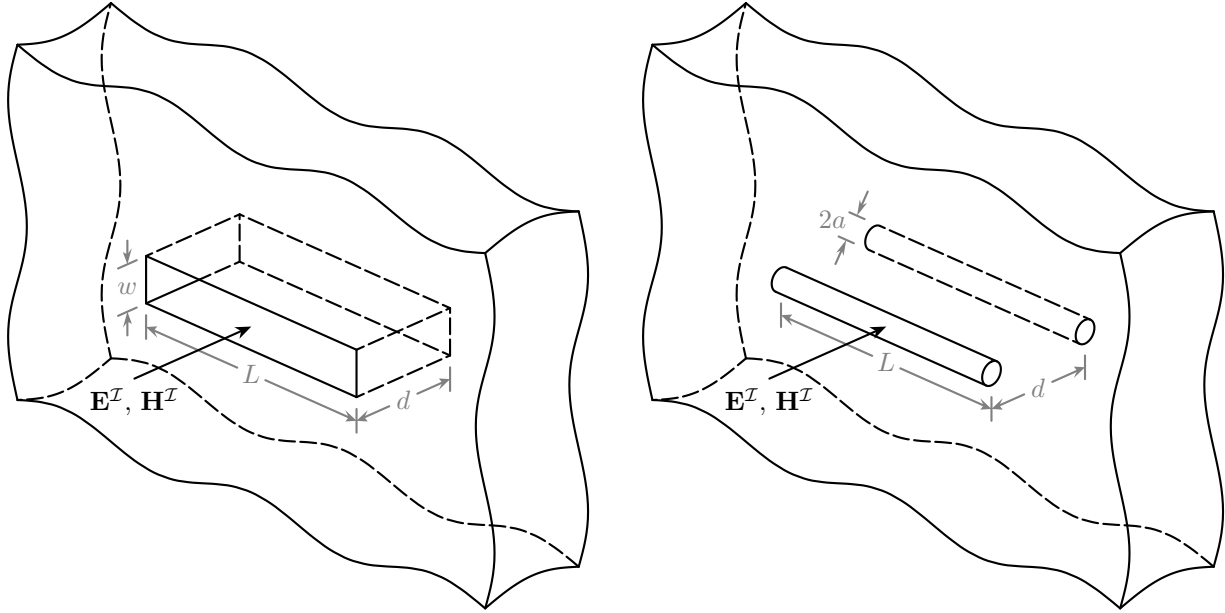


Figure 1: Left: an excerpt of an exterior surface of an otherwise closed scatterer, which contains a slot. The slot connects the exterior domain to an interior cavity. Right: the slot is replaced with two wires located at the openings of the slot.

In this work, we focus on a slot model that can accommodate an arbitrary depth, as described in [12]. This model differs from the *thick* (i.e., small-depth) slot model considered in [44] that is described in [47–50]. Unlike the thick slot model, which assumes the magnetic currents along the two aperture wires are equal and opposite due to the small depth, the model considered in this paper permits these currents to differ, and therefore assigns a separate set of degrees of freedom to the currents on each wire.

As described in [42], electromagnetic SIEs incur numerical error due to curved surfaces being approximated by planar elements (domain-discretization error), the solution being approximated as a linear combination of a finite number of basis functions (solution-discretization error), and the integration being approximately evaluated using quadrature rules (numerical-integration error). In this paper, we isolate and measure the solution-discretization error and numerical-integration error. To isolate the two error sources, we manufacture the electric surface current density, which yields a source term that we can incorporate as a manufactured incident field. Given the manufactured electric surface current, we can analytically solve the continuous slot equation to obtain an exact, known solution for the magnetic current. This exact solution eliminates the need for the MMS source term in the slot equation. However, the magnetic current solution takes the form of an infinite sine series, which must be truncated carefully to prevent the series truncation error from contaminating convergence studies for both sources of error.

This paper is organized as follows. In Section 2, we describe the EFIE and the arbitrary-depth slot model. In Section 3, we provide the details for their discretization. In Section 4, we discuss our code-verification approaches for these equations. In Section 5, we demonstrate the effectiveness of our approaches for several different configurations. In Section 6, we summarize this work.

## 2. Governing Equations

We consider an electromagnetic scatterer that encloses a cavity. The exterior of the scatterer and the cavity are connected by a narrow, rectangularly prismatic slot, as shown in Figure 1. The width  $w$  of the slot is assumed to be much smaller than its length  $L$ . However, unlike the slot considered in [44], the depth  $d$  of the slot is of an arbitrary extent. Aside from the slot, the exterior of the scatterer and the interior of the cavity are modeled as distinct closed surfaces. The electric current on the exterior and interior surfaces is modeled using the electric-field integral equation for a good, but imperfect, electric conductor. The slot is modeled by wires at its openings on the exterior and interior surfaces using transmission line theory. These

wires have a small but finite radius  $a$  and carry magnetic current. Through this approach, the interior and exterior surfaces do not directly interact. Instead, the magnetic current on the exterior wire interacts with the electric current on the exterior surface and the magnetic current on the interior wire interacts with the electric current on the interior surface. The wires additionally interact with each other through a waveguide model.

### 2.1. Preliminaries

For a medium with finite electrical conductivity  $\sigma$  and employing the Lorenz gauge condition and the continuity equation, the electric field  $\mathbf{E}$  and magnetic field  $\mathbf{H}$  can be expressed in terms of the magnetic vector potential  $\mathbf{A}$  and electric vector potential  $\mathbf{F}$  in time-harmonic form as [2, Chap. 6]

$$\mathbf{E} = -\left(\frac{j}{\omega\mu\epsilon}\nabla(\nabla\cdot\mathbf{A}) + j\omega\mathbf{A} + \frac{1}{\epsilon}\nabla\times\mathbf{F}\right), \quad (1)$$

$$\mathbf{H} = \frac{1}{\mu}\nabla\times\mathbf{A} - j\omega\mathbf{F} - \frac{j}{\omega\mu\epsilon}\nabla(\nabla\cdot\mathbf{F}), \quad (2)$$

where  $\omega$  is the angular frequency. The complex permittivity  $\epsilon$  is defined by

$$\epsilon = \epsilon' - j\frac{\sigma}{\omega},$$

and  $\mu$ ,  $\sigma$ , and  $\epsilon'$  are the permeability, conductivity, and real part of the permittivity of the medium.

For an electric conductor with large but finite conductivity, the surface impedance boundary condition is [2, Chap. 14]

$$\mathbf{E} - (\mathbf{E}\cdot\mathbf{n})\mathbf{n} = Z_s\mathbf{n}\times\mathbf{H}, \quad (3)$$

where  $Z_s$  is the resistive surface impedance of the conductor, and  $\mathbf{n}$  is the unit vector normal to the conductor surface that points away from the conductor.

### 2.2. The Electromagnetic Scatterer

The scatterer is modeled as a good electric conductor, and the electric-field integral equation is evaluated separately on the exterior and interior surfaces of the scatterer. The scattered electric field  $\mathbf{E}^S$  due to induced electric and magnetic surface currents on a scatterer is given by (1), where the magnetic vector potential  $\mathbf{A}$  is defined by

$$\mathbf{A}(\mathbf{x}) = \mu \int_{S'} \mathbf{J}(\mathbf{x}')G(\mathbf{x}, \mathbf{x}')dS', \quad (4)$$

and the electric vector potential  $\mathbf{F}$  is defined by

$$\mathbf{F}(\mathbf{x}) = \epsilon \int_{S'} \mathbf{M}(\mathbf{x}')G(\mathbf{x}, \mathbf{x}')dS'. \quad (5)$$

In (4) and (5), the integration domain  $S' = S$  is the exterior or interior surface of the scatterer, and the prime notation is introduced here to distinguish the source and test integration domains later in this section. Additionally,  $\mathbf{J}$  is the electric surface current density,  $\mathbf{M}$  is the magnetic surface current density,  $\mu$  and  $\epsilon$  describe the surrounding medium, and  $G$  is the Green's function

$$G(\mathbf{x}, \mathbf{x}') = \frac{e^{-jkR}}{4\pi R}, \quad (6)$$

where  $R = \|\mathbf{R}\|_2$ ,  $\mathbf{R} = \mathbf{x} - \mathbf{x}'$ , and  $k = \omega\sqrt{\mu\epsilon}$  is the wavenumber.

The total electric field  $\mathbf{E}$  is the sum of  $\mathbf{E}^S$  and the incident electric field  $\mathbf{E}^I$ , which induces  $\mathbf{J}$  and  $\mathbf{M}$ :

$$\mathbf{E} = \mathbf{E}^S + \mathbf{E}^I. \quad (7)$$

Inserting (7) into (3), taking the cross product of  $\mathbf{n}$  with (3), and noting that  $\mathbf{J} = \mathbf{n} \times \mathbf{H}$  yields

$$\mathbf{n} \times \mathbf{E} = \mathbf{n} \times (\mathbf{E}^S + \mathbf{E}^T) = Z_s \mathbf{n} \times \mathbf{J}. \quad (8)$$

Inserting (1) into (8) yields [44]

$$\begin{aligned} \mathbf{n} \times \left( \frac{j}{\omega\epsilon} \int_{S'} \nabla' \cdot \mathbf{J}(\mathbf{x}') \nabla G(\mathbf{x}, \mathbf{x}') dS' + j\omega\mu \int_{S'} \mathbf{J}(\mathbf{x}') G(\mathbf{x}, \mathbf{x}') dS' \right. \\ \left. + \int_{S'} \mathbf{M}(\mathbf{x}') \times \nabla' G(\mathbf{x}, \mathbf{x}') dS' + Z_s \mathbf{J} \right) + \frac{1}{2} \mathbf{M} = \mathbf{n} \times \mathbf{E}^T. \end{aligned} \quad (9)$$

We project (9) onto an appropriate space  $\mathbb{V}$  containing vector fields that are tangent to  $S$ . Integrating by parts yields the variational form of the EFIE: find  $\mathbf{J}, \mathbf{M} \in \mathbb{V}$ , such that

$$\begin{aligned} -\frac{j}{\epsilon\omega} \int_S \nabla \cdot \bar{\mathbf{v}}(\mathbf{x}) \int_{S'} \nabla' \cdot \mathbf{J}(\mathbf{x}') G(\mathbf{x}, \mathbf{x}') dS' dS + j\omega\mu \int_S \bar{\mathbf{v}}(\mathbf{x}) \cdot \int_{S'} \mathbf{J}(\mathbf{x}') G(\mathbf{x}, \mathbf{x}') dS' dS \\ - \frac{1}{2} \int_S \bar{\mathbf{v}} \cdot (\mathbf{n} \times \mathbf{M}) dS + \int_S \bar{\mathbf{v}}(\mathbf{x}) \cdot \int_{S'} \mathbf{M}(\mathbf{x}') \times \nabla' G(\mathbf{x}, \mathbf{x}') dS' dS + Z_s \int_S \bar{\mathbf{v}} \cdot \mathbf{J} dS = \int_S \bar{\mathbf{v}} \cdot \mathbf{E}^T dS \end{aligned} \quad (10)$$

for all  $\mathbf{v} \in \mathbb{V}$ , where the overbar denotes complex conjugation.

As described briefly in the beginning of this section and in detail in [44], the slot opening on each surface is modeled by a wire characterized by a small effective radius  $a$ . As a result, the surface magnetic current density  $\mathbf{M}$  is replaced by the filament magnetic current of the wire  $\mathbf{I}_m(s) = I_m(s)\mathbf{s}$ , where  $s \in [0, L]$  denotes the position along the wire, and  $\mathbf{s}$  denotes the direction of the wire. Therefore, (10) is written as: find  $\mathbf{J} \in \mathbb{V}$  and  $\mathbf{I}_m \in \mathbb{V}^m$ , such that

$$\begin{aligned} -\frac{j}{\omega\epsilon} \int_S \nabla \cdot \bar{\mathbf{v}}(\mathbf{x}) \int_{S'} \nabla' \cdot \mathbf{J}(\mathbf{x}') G(\mathbf{x}, \mathbf{x}') dS' dS + j\omega\mu \int_S \bar{\mathbf{v}}(\mathbf{x}) \cdot \int_{S'} \mathbf{J}(\mathbf{x}') G(\mathbf{x}, \mathbf{x}') dS' dS \\ - \frac{1}{4} \int_0^L \bar{\mathbf{v}} \cdot (\mathbf{n} \times \mathbf{I}_m) ds + \frac{1}{4\pi} \int_S \bar{\mathbf{v}}(\mathbf{x}) \cdot \int_0^L \mathbf{I}_m(s') \times \int_0^{2\pi} \nabla' G(\mathbf{x}, \mathbf{x}') d\phi' ds' dS + Z_s \int_S \bar{\mathbf{v}} \cdot \mathbf{J} dS = \int_S \bar{\mathbf{v}} \cdot \mathbf{E}^T dS \end{aligned} \quad (11)$$

for all  $\mathbf{v} \in \mathbb{V}$ , where  $\phi$  is the azimuthal angle and  $\mathbb{V}^m$  is an appropriate space containing vector fields that are located on and tangent to the wire and vanish at  $s = 0$  and  $s = L$ . We can write (11) more succinctly as

$$a_{\mathcal{E}, \mathcal{E}}(\mathbf{J}, \mathbf{v}) + a_{\mathcal{E}, \mathcal{M}}(\mathbf{I}_m, \mathbf{v}) = b_{\mathcal{E}}(\mathbf{E}^T, \mathbf{v}), \quad (12)$$

where the sesquilinear forms and inner product are defined by

$$\begin{aligned} a_{\mathcal{E}, \mathcal{E}}(\mathbf{u}, \mathbf{v}) = -\frac{j}{\omega\epsilon} \int_S \nabla \cdot \bar{\mathbf{v}}(\mathbf{x}) \int_{S'} \nabla' \cdot \mathbf{u}(\mathbf{x}') G(\mathbf{x}, \mathbf{x}') dS' dS + j\omega\mu \int_S \bar{\mathbf{v}}(\mathbf{x}) \cdot \int_{S'} \mathbf{u}(\mathbf{x}') G(\mathbf{x}, \mathbf{x}') dS' dS \\ + Z_s \int_S \bar{\mathbf{v}}(\mathbf{x}) \cdot \mathbf{u}(\mathbf{x}) dS, \end{aligned} \quad (13)$$

$$a_{\mathcal{E}, \mathcal{M}}(\mathbf{u}, \mathbf{v}) = -\frac{1}{4} \int_0^L \bar{\mathbf{v}}(\mathbf{x}) \cdot [\mathbf{n}(\mathbf{x}) \times \mathbf{u}(s)] ds + \frac{1}{4\pi} \int_S \bar{\mathbf{v}}(\mathbf{x}) \cdot \int_0^L \mathbf{u}(s') \times \int_0^{2\pi} \nabla' G(\mathbf{x}, \mathbf{x}') d\phi' ds' dS, \quad (14)$$

$$b_{\mathcal{E}}(\mathbf{u}, \mathbf{v}) = \int_S \bar{\mathbf{v}}(\mathbf{x}) \cdot \mathbf{u}(\mathbf{x}) dS.$$

### 2.3. The Slot Model

The slot is modeled as a rectangular waveguide with an electrically small width [12]. The waveguide supports transverse magnetic modes in the widthwise direction, such that  $\mathbf{F} = \mathbf{0}$  [2, Chap. 6]. As a result, (1) and (2) reduce to

$$\mathbf{E} = -\left( \frac{j}{\omega\mu\epsilon} \nabla(\nabla \cdot \mathbf{A}) + j\omega\mathbf{A} \right), \quad (15)$$

$$\mathbf{H} = \frac{1}{\mu} \nabla \times \mathbf{A}. \quad (16)$$

In the absence of sources,  $\mathbf{E}$  and  $\mathbf{H}$  can be related through the Ampère–Maxwell equation

$$\nabla \times \mathbf{H} = j\omega\epsilon\mathbf{E}. \quad (17)$$

Inserting (15) and (16) into (17) yields the Helmholtz equation

$$\Delta \mathbf{A} + k^2 \mathbf{A} = \mathbf{0}. \quad (18)$$

For notational convenience, we temporarily assume the rectangular waveguide is oriented such that the width, depth, and length are aligned with the  $x$ -,  $y$ -, and  $z$ -axes. Because the widthwise dimension of the slot is assumed to be much smaller than the other two dimensions, the magnetic field is modeled as transverse magnetic to the widthwise direction. Therefore, the magnetic vector potential takes the form  $\mathbf{A} = A\mathbf{e}_x$  [12], such that (15) becomes

$$E_x = -\frac{j}{\omega\mu\epsilon} \left( \frac{\partial^2}{\partial x^2} + k^2 \right) A, \quad E_y = -\frac{j}{\omega\mu\epsilon} \frac{\partial^2}{\partial x \partial y} A, \quad E_z = -\frac{j}{\omega\mu\epsilon} \frac{\partial^2}{\partial x \partial z} A; \quad (19)$$

(16) becomes

$$H_x = 0, \quad H_y = \frac{1}{\mu} \frac{\partial}{\partial z} A, \quad H_z = -\frac{1}{\mu} \frac{\partial}{\partial y} A; \quad (20)$$

and (18) becomes

$$\Delta A + k^2 A = 0. \quad (21)$$

Equation (21) is solved using separation of variables with  $A$  taking the form

$$A(x, y, z) = A_x(x)A_y(y)A_z(z), \quad (22)$$

where

$$A_\alpha(\alpha) = C_\alpha \cos(\beta_\alpha \alpha) + D_\alpha \sin(\beta_\alpha \alpha) \quad (23)$$

for  $\alpha \in \{x, y, z\}$ .  $\beta_\alpha$  is the propagation constant in the  $\alpha$ -direction, and

$$k^2 = \beta_x^2 + \beta_y^2 + \beta_z^2. \quad (24)$$

With the electrically small width,  $w \operatorname{Re}(\beta_x) \ll 1$ , such that, for  $x \in [-w/2, w/2]$ ,  $|\cos(\beta_x x)| \gg |\sin(\beta_x x)|$  in  $A_x(x)$  [12], such that we can set  $D_x = 0$  in (23). The conducting surface of the scatterer yields the surface impedance boundary condition (3) for the medium.

### 2.3.1. Widthwise Dependency

For  $x = \pm w/2$ ,  $\mathbf{n} = \mp \mathbf{e}_x$ , and, from (3),  $E_y = \pm Z_s H_z$  and  $E_z = \mp Z_s H_y$ , such that, from (19) and (20), these boundary conditions are satisfied by

$$\frac{d}{dx} A_x(\pm w/2) = \mp j Z_s \omega \epsilon A_x(\pm w/2). \quad (25)$$

Equation (25) is satisfied by

$$\beta_x \tan(\beta_x w/2) = j Z_s \omega \epsilon. \quad (26)$$

Noting the electrically small width,  $\beta_x \tan(\beta_x w/2) \approx w\beta_x^2/2$ , such that (26) can be approximated by [12]

$$\beta_x^2 \approx \frac{2j Z_s \omega \epsilon}{w}. \quad (27)$$

Ignoring the constant factor  $C_x$  in (23), we can approximate  $A_x$  and  $d^2 A_x/dx^2$  by [12]

$$A_x(x) = \cos \beta_x x \approx 1, \quad \frac{d^2 A_x}{dx^2} = -\beta_x^2 A_x(x) \approx -\beta_x^2. \quad (28)$$

### 2.3.2. Lengthwise Dependency

At  $z = \{0, L\}$ , the electrically small width permits the conducting surface to be approximated as a perfect electric conductor, such that  $H_z = 0$  [12]. From (20),

$$A_z(0) = A_z(L) = 0. \quad (29)$$

Equation (29) is satisfied by modes proportional to

$$A_{z_p}(z) = \sin(\beta_{z_p} z) \quad (30)$$

where

$$\beta_{z_p} = \frac{p\pi}{L} \quad (31)$$

for  $p \in \mathbb{N}_1$ .

### 2.3.3. Depthwise Dependency

With (28) and (30), (22) becomes

$$A(y, z) = \sum_{p=1}^{\infty} A_p(y, z), \quad (32)$$

where

$$A_p(y, z) = [C_{y_p} \cos(\beta_{y_p} y) + D_{y_p} \sin(\beta_{y_p} y)] \sin\left(\frac{p\pi z}{L}\right). \quad (33)$$

From [47], at the inlet and outlet of the slot, the filament line-source magnetic current flowing along the wires in the lengthwise dimension is related to the voltage across the slot by

$$\pm I_m^\pm(z) = 2V^\pm(z), \quad (34)$$

where the superscript  $(-)$  denotes the inlet ( $y = -d/2$ ), and the superscript  $(+)$  denotes the outlet ( $y = d/2$ ). The factor of 2 in (34) is due to the convention used in [12] and [47], where the magnetic current is doubled due to reflection in an infinite conducting plane (cf. [2, Chap. 7]). The voltage across the slot is related to the electric field across the slot by [12]

$$V^\pm(z) = wE_x(\pm d/2, z). \quad (35)$$

From (32)–(35) and (19),

$$\pm I_m^\pm(z)/2 = \frac{-jw(k^2 - \beta_x^2)}{\omega\mu\epsilon} \sum_{p=1}^{\infty} [C_{y_p} \cos(\beta_{y_p} d/2) \pm D_{y_p} \sin(\beta_{y_p} d/2)] \sin\left(\frac{p\pi z}{L}\right). \quad (36)$$

Multiplying (36) by  $\sin(q\pi z/L)$ , integrating with respect to  $z$ , and noting that

$$\int_0^L \sin\left(\frac{p\pi z}{L}\right) \sin\left(\frac{q\pi z}{L}\right) dz = \frac{L}{2} \delta_{pq}, \quad (37)$$

where  $\delta_{pq}$  is the Kronecker delta, yields

$$\pm \frac{1}{2} \int_0^L I_m^\pm(z) \sin\left(\frac{p\pi z}{L}\right) dz = \frac{-jwL(k^2 - \beta_x^2)}{2\omega\mu\epsilon} [C_{y_p} \cos(\beta_{y_p} d/2) \pm D_{y_p} \sin(\beta_{y_p} d/2)]. \quad (38)$$

Adding the positive version of (38) to the negative version of (38) yields

$$C_{y_p} = \frac{j\omega\mu\epsilon}{wL(k^2 - \beta_x^2) \cos(\beta_{y_p} d/2)} \int_0^L \frac{1}{2} [I_m^+(z) - I_m^-(z)] \sin\left(\frac{p\pi z}{L}\right) dz. \quad (39)$$

Subtracting the negative version of (38) from the positive version of (38) yields

$$D_{y_p} = \frac{j\omega\mu\epsilon}{wL(k^2 - \beta_x^2) \sin(\beta_{y_p} d/2)} \int_0^L \frac{1}{2} [I_m^+(z) + I_m^-(z)] \sin\left(\frac{p\pi z}{L}\right) dz. \quad (40)$$

With the expressions for  $\beta_x$  (27) and  $\beta_{z_p}$  (31),  $\beta_{y_p}$  can be obtained from (24):

$$\beta_{y_p}^2 = k^2 - \beta_x^2 - \beta_{z_p}^2. \quad (41)$$

From (39), (40), and (41),  $A$  (32) and, consequently,  $\mathbf{H}$  are expressed in terms of  $I_m$ .

### 2.3.4. The Slot Equation

To relate  $I_m$  and  $\mathbf{J}$ , we consider the magnetic field at the openings of the slot, where the sum of the magnetic field due to  $\mathbf{J}$  on the scatterer and the waveguide magnetic field is zero:

$$\mathbf{J}^\pm \times \mathbf{n}^\pm - H_s(\pm d/2, s)\mathbf{s} = \mathbf{0}. \quad (42)$$

From (20) and (32),

$$\begin{aligned} H_s(\pm d/2, s) &= -\frac{1}{\mu} \frac{\partial}{\partial y} A(\pm d/2, s) \\ &= -\frac{j\omega\epsilon}{2wL(k^2 - \beta_x^2)} \sum_{p=1}^{\infty} \beta_{y_p} \int_0^L \sin\left(\frac{p\pi s}{L}\right) \sin\left(\frac{p\pi s'}{L}\right) \times \\ &\quad (\pm [I_m^-(s') - I_m^+(s')] \tan(\beta_{y_p} d/2) + [I_m^+(s') + I_m^-(s')] \cot(\beta_{y_p} d/2)) ds'. \end{aligned}$$

Additionally,  $I_m(0) = I_m(L) = 0$ .

We project (42) onto  $\mathbb{V}^m$  to obtain the variational form of the slot equation: find  $\mathbf{I}_m = I_m(s)\mathbf{s} \in \mathbb{V}^m$  and  $\mathbf{J} \in \mathbb{V}$ , such that

$$\begin{aligned} \int_0^L \bar{\mathbf{v}}^m \cdot (\mathbf{J}^\pm \times \mathbf{n}^\pm) ds + \frac{j\omega\epsilon}{2wL(k^2 - \beta_x^2)} \sum_{p=1}^{\infty} \beta_{y_p} \int_0^L (\bar{\mathbf{v}}^m(s) \cdot \mathbf{s}) \sin\left(\frac{p\pi s}{L}\right) ds \int_0^L \sin\left(\frac{p\pi s'}{L}\right) \times \\ (\pm [I_m^-(s') - I_m^+(s')] \tan(\beta_{y_p} d/2) + [I_m^+(s') + I_m^-(s')] \cot(\beta_{y_p} d/2)) ds' = 0 \end{aligned} \quad (43)$$

for all  $\mathbf{v}^m \in \mathbb{V}^m$ . We can write (43) more succinctly as

$$a_{\mathcal{M}, \mathcal{E}}(\mathbf{J}, \mathbf{v}^m) + a_{\mathcal{M}, \mathcal{M}}(\mathbf{I}_m, \mathbf{v}^m) = 0, \quad (44)$$

where the sesquilinear forms are defined by

$$\begin{aligned} a_{\mathcal{M}, \mathcal{E}}(\mathbf{u}, \mathbf{v}) &= \int_0^L \bar{\mathbf{v}}(s) \cdot [\mathbf{u}(\mathbf{x}) \times \mathbf{n}(\mathbf{x})] ds, \\ a_{\tilde{\mathcal{M}}, \mathcal{M}}(\mathbf{u}, \mathbf{v}) &= \frac{j\omega\epsilon}{2wL(k^2 - \beta_x^2)} \sum_{p=1}^{\infty} \beta_{y_p} F^p(\bar{\mathbf{v}}) F^p(\mathbf{u}) \left( -\tan(\beta_{y_p} d/2) + \cot(\beta_{y_p} d/2) \right), \end{aligned} \quad (45)$$

$$a_{\not\sim \mathcal{M}, \mathcal{M}}(\mathbf{u}, \mathbf{v}) = \frac{j\omega\epsilon}{2wL(k^2 - \beta_x^2)} \sum_{p=1}^{\infty} \beta_{y_p} F^p(\bar{\mathbf{v}}) F^p(\mathbf{u}) \left( +\tan(\beta_{y_p} d/2) + \cot(\beta_{y_p} d/2) \right), \quad (46)$$

where

$$F^p(\mathbf{u}) = \int_0^L (\mathbf{u}(s) \cdot \mathbf{s}) \sin\left(\frac{p\pi s}{L}\right) ds.$$

For  $a_{\mathcal{M}, \mathcal{M}}$ , the superscript ( $\sim$ ) indicates  $\mathbf{u}$  and  $\mathbf{v}$  are located at the same opening, whereas the superscript ( $\not\sim$ ) indicates opposite openings.

### 3. Discretization

To solve (12) and (44), we discretize  $S$  with a mesh composed of triangular elements and approximate  $\mathbf{J}$  with  $\mathbf{J}_h$  using the Rao–Wilton–Glisson (RWG) basis functions  $\mathbf{\Lambda}_j(\mathbf{x})$  [51]:

$$\mathbf{J}_h(\mathbf{x}) = \sum_{j=1}^{n_b} J_j \mathbf{\Lambda}_j(\mathbf{x}), \quad (47)$$

where  $n_b$  is the number of RWG basis functions. The RWG basis functions are second-order accurate, and the solution is considered most accurate at the edge midpoints [52, pp. 155–156]; therefore, we measure the solution at the midpoints.

We similarly discretize each wire with one-dimensional bar elements and approximate  $\mathbf{I}_m$  with  $\mathbf{I}_h$  using a one-dimensional analog to the RWG basis functions  $\mathbf{\Lambda}_j^m(s)$ :

$$\mathbf{I}_h(s) = \sum_{j=1}^{n_b^m} I_j \mathbf{\Lambda}_j^m(s), \quad (48)$$

where  $n_b^m$  is the number of one-dimensional basis functions.

Defining  $\mathbb{V}_h$  to be the span of RWG basis functions and  $\mathbb{V}_h^m$  to be the span of the one-dimensional basis functions, the Galerkin approximation of (12) and (44) is now: find  $\mathbf{J}_h \in \mathbb{V}_h$  and  $\mathbf{I}_h \in \mathbb{V}_h^m$ , such that

$$a_{\mathcal{E},\mathcal{E}}(\mathbf{J}_h, \mathbf{\Lambda}_i) + a_{\mathcal{E},\mathcal{M}}(\mathbf{I}_h, \mathbf{\Lambda}_i) = b_{\mathcal{E}}(\mathbf{E}^{\mathcal{I}}, \mathbf{\Lambda}_i) \quad (49)$$

for  $i = 1, \dots, n_b$ , and

$$a_{\mathcal{M},\mathcal{E}}(\mathbf{J}_h, \mathbf{\Lambda}_i^m) + a_{\mathcal{M},\mathcal{M}}(\mathbf{I}_h, \mathbf{\Lambda}_i^m) = 0 \quad (50)$$

for  $i = 1, \dots, n_b^m$ .

We evaluate (49) on the exterior (−) and interior (+) surfaces of the scatterer, such that there are  $n_b = n_b^- + n_b^+$  unknowns for  $\mathbf{J}_h$ . Similarly, (50) is evaluated for the wires on the exterior and interior surfaces. The thick slot model described in [44] models  $\mathbf{I}_m$  as equal and opposite at the corresponding locations on the interior and exterior surface wires, reducing the number of unknowns for  $\mathbf{I}_h$  to  $n_b^{m-}$  or  $n_b^{m+}$ . On the other hand, in this work, we model the slot as having an arbitrary depth, such that the two wires are modeled with separate unknowns but with the same number of unknowns per wire; consequently, there are  $n_b^m = n_b^{m-} + n_b^{m+}$  unknowns for  $\mathbf{I}_h$ , and  $n_b^{m-} = n_b^{m+}$ .

The discretized system of equations can be written in matrix–vector form as

$$\mathbf{Z}\mathcal{J}^h = \mathbf{V}. \quad (51)$$

The impedance matrix  $\mathbf{Z}$  is given by

$$\mathbf{Z} = \begin{bmatrix} \mathbf{A}^- & \mathbf{0} & \mathbf{B}^- & \mathbf{0} \\ \mathbf{0} & \mathbf{A}^+ & \mathbf{0} & \mathbf{B}^+ \\ \mathbf{C}^- & \mathbf{0} & \mathbf{D}_{\sim}^- & \mathbf{D}_{\not\sim}^- \\ \mathbf{0} & \mathbf{C}^+ & \mathbf{D}_{\sim}^+ & \mathbf{D}_{\not\sim}^+ \end{bmatrix} \in \mathbb{C}^{(n_b+n_b^m) \times (n_b+n_b^m)},$$

where

$$\begin{aligned} A_{i,j} &= a_{\mathcal{E},\mathcal{E}}(\mathbf{\Lambda}_j, \mathbf{\Lambda}_i), & \mathbf{A}^- &\in \mathbb{C}^{n_b^- \times n_b^-}, & \mathbf{A}^+ &\in \mathbb{C}^{n_b^+ \times n_b^+}, \\ B_{i,j} &= a_{\mathcal{E},\mathcal{M}}(\mathbf{\Lambda}_j^m, \mathbf{\Lambda}_i), & \mathbf{B}^- &\in \mathbb{C}^{n_b^- \times n_b^{m-}}, & \mathbf{B}^+ &\in \mathbb{C}^{n_b^+ \times n_b^{m+}}, \\ C_{i,j} &= a_{\mathcal{M},\mathcal{E}}(\mathbf{\Lambda}_j, \mathbf{\Lambda}_i^m), & \mathbf{C}^- &\in \mathbb{R}^{n_b^- \times n_b^-}, & \mathbf{C}^+ &\in \mathbb{R}^{n_b^+ \times n_b^+}, \\ D_{\sim i,j} &= a_{\sim \mathcal{M},\mathcal{M}}(\mathbf{\Lambda}_j^m, \mathbf{\Lambda}_i^m), & \mathbf{D}_{\sim}^- &\in \mathbb{C}^{n_b^{m-} \times n_b^{m-}}, & \mathbf{D}_{\sim}^+ &\in \mathbb{C}^{n_b^{m+} \times n_b^{m+}}, \\ D_{\not\sim i,j} &= a_{\not\sim \mathcal{M},\mathcal{M}}(\mathbf{\Lambda}_j^m, \mathbf{\Lambda}_i^m), & \mathbf{D}_{\not\sim}^+ &\in \mathbb{C}^{n_b^{m+} \times n_b^{m-}}, & \mathbf{D}_{\not\sim}^- &\in \mathbb{C}^{n_b^{m-} \times n_b^{m+}}. \end{aligned}$$



$\mathbf{Z}$  can be written more compactly as

$$\mathbf{Z} = \begin{bmatrix} \mathbf{A} & \mathbf{B} \\ \mathbf{C} & \mathbf{D} \end{bmatrix}, \quad (52)$$

where

$$\begin{aligned} \mathbf{A} &= \begin{bmatrix} \mathbf{A}^- & \mathbf{0} \\ \mathbf{0} & \mathbf{A}^+ \end{bmatrix} \in \mathbb{C}^{n_b \times n_b}, & \mathbf{B} &= \begin{bmatrix} \mathbf{B}^- & \mathbf{0} \\ \mathbf{0} & \mathbf{B}^+ \end{bmatrix} \in \mathbb{C}^{n_b \times n_b^m}, \\ \mathbf{C} &= \begin{bmatrix} \mathbf{C}^- & \mathbf{0} \\ \mathbf{0} & \mathbf{C}^+ \end{bmatrix} \in \mathbb{R}^{n_b^m \times n_b}, & \mathbf{D} &= \begin{bmatrix} \mathbf{D}_{\sim}^- & \mathbf{D}_{\not\sim}^- \\ \mathbf{D}_{\not\sim}^+ & \mathbf{D}_{\sim}^+ \end{bmatrix} \in \mathbb{C}^{n_b^m \times n_b^m}. \end{aligned}$$

The solution vector  $\mathcal{J}^h$ , which contains the coefficients used to construct  $\mathbf{J}_h$  (47) and  $\mathbf{I}_h$  (48), is given by

$$\mathcal{J}^h = \begin{Bmatrix} \mathbf{J}^{h-} \\ \mathbf{J}^{h+} \\ \mathbf{I}^{h-} \\ \mathbf{I}^{h+} \end{Bmatrix} \in \mathbb{C}^{n_b+n_b^m},$$

where

$$\begin{aligned} J_j^h &= J_j, & \mathbf{J}^{h-} &\in \mathbb{C}^{n_b^-}, & \mathbf{J}^{h+} &\in \mathbb{C}^{n_b^+}, \\ I_j^h &= I_j, & \mathbf{I}^{h-} &\in \mathbb{C}^{n_b^m^-}, & \mathbf{I}^{h+} &\in \mathbb{C}^{n_b^m^+}. \end{aligned}$$

$\mathcal{J}^h$  can be written more compactly as

$$\mathcal{J}^h = \begin{Bmatrix} \mathbf{J}^h \\ \mathbf{I}^h \end{Bmatrix},$$

where

$$\mathbf{J}^h = \begin{Bmatrix} \mathbf{J}^{h-} \\ \mathbf{J}^{h+} \end{Bmatrix} \in \mathbb{C}^{n_b}, \quad \mathbf{I}^h = \begin{Bmatrix} \mathbf{I}^{h-} \\ \mathbf{I}^{h+} \end{Bmatrix} \in \mathbb{C}^{n_b^m}.$$

Finally, the excitation vector  $\mathbf{V}$  is given by

$$\mathbf{V} = \begin{Bmatrix} \mathbf{V}^{\mathcal{E}^-} \\ \mathbf{V}^{\mathcal{E}^+} \\ \mathbf{0} \end{Bmatrix} \in \mathbb{C}^{n_b+n_b^m},$$

where

$$V_i^{\mathcal{E}} = b_{\mathcal{E}}(\mathbf{E}^{\mathcal{I}}, \boldsymbol{\Lambda}_i), \quad \mathbf{V}^{\mathcal{E}^-} \in \mathbb{C}^{n_b^-}, \quad \mathbf{V}^{\mathcal{E}^+} \in \mathbb{C}^{n_b^+}.$$

$\mathbf{V}$  can be written more compactly as

$$\mathbf{V} = \begin{Bmatrix} \mathbf{V}^{\mathcal{E}} \\ \mathbf{0} \end{Bmatrix},$$

where

$$\mathbf{V}^{\mathcal{E}} = \begin{Bmatrix} \mathbf{V}^{\mathcal{E}^-} \\ \mathbf{V}^{\mathcal{E}^+} \end{Bmatrix} \in \mathbb{C}^{n_b}.$$

#### 4. Manufactured Solutions

The residual functionals for the surfaces and wires are

$$r_{\mathcal{E}_i}(\mathbf{u}, \mathbf{v}) = a_{\mathcal{E},\mathcal{E}}(\mathbf{u}, \boldsymbol{\Lambda}_i) + a_{\mathcal{E},\mathcal{M}}(\mathbf{v}, \boldsymbol{\Lambda}_i) - b_{\mathcal{E}}(\mathbf{E}^{\mathcal{I}}, \boldsymbol{\Lambda}_i), \quad (53)$$

$$r_{\mathcal{M}_i}(\mathbf{u}, \mathbf{v}) = a_{\mathcal{M},\mathcal{E}}(\mathbf{u}, \boldsymbol{\Lambda}_i^m) + a_{\mathcal{M},\mathcal{M}}(\mathbf{v}, \boldsymbol{\Lambda}_i^m). \quad (54)$$

Using (53) and (54), the variational forms of (12) and (44) are

$$r_{\mathcal{E}_i}(\mathbf{J}, \mathbf{I}_m) = a_{\mathcal{E},\mathcal{E}}(\mathbf{J}, \boldsymbol{\Lambda}_i) + a_{\mathcal{E},\mathcal{M}}(\mathbf{I}_m, \boldsymbol{\Lambda}_i) - b_{\mathcal{E}}(\mathbf{E}^{\mathcal{I}}, \boldsymbol{\Lambda}_i) = 0, \quad (55)$$

$$r_{\mathcal{M}_i}(\mathbf{J}, \mathbf{I}_m) = a_{\mathcal{M},\mathcal{E}}(\mathbf{J}, \boldsymbol{\Lambda}_i^m) + a_{\mathcal{M},\mathcal{M}}(\mathbf{I}_m, \boldsymbol{\Lambda}_i^m) = 0. \quad (56)$$

Similarly, in terms of (53) and (54), the discretized problems in (49) and (50) are

$$r_{\mathcal{E}_i}(\mathbf{J}_h, \mathbf{I}_h) = a_{\mathcal{E},\mathcal{E}}(\mathbf{J}_h, \boldsymbol{\Lambda}_i) + a_{\mathcal{E},\mathcal{M}}(\mathbf{I}_h, \boldsymbol{\Lambda}_i) - b_{\mathcal{E}}(\mathbf{E}^{\mathcal{I}}, \boldsymbol{\Lambda}_i) = 0, \quad (57)$$

$$r_{\mathcal{M}_i}(\mathbf{J}_h, \mathbf{I}_h) = a_{\mathcal{M},\mathcal{E}}(\mathbf{J}_h, \boldsymbol{\Lambda}_i^m) + a_{\mathcal{M},\mathcal{M}}(\mathbf{I}_h, \boldsymbol{\Lambda}_i^m) = 0. \quad (58)$$

The method of manufactured solutions modifies (57) and (58) to be

$$r_{\mathcal{E}_i}(\mathbf{J}_h, \mathbf{I}_h) = r_{\mathcal{E}_i}(\mathbf{J}_{\text{MS}}, \mathbf{I}_{\text{MS}}), \quad (59)$$

$$r_{\mathcal{M}_i}(\mathbf{J}_h, \mathbf{I}_h) = r_{\mathcal{M}_i}(\mathbf{J}_{\text{MS}}, \mathbf{I}_{\text{MS}}), \quad (60)$$

where  $\mathbf{J}_{\text{MS}}$  and  $\mathbf{I}_{\text{MS}}$  are the manufactured solutions, and  $r_{\mathcal{E}}(\mathbf{J}_{\text{MS}}, \mathbf{I}_{\text{MS}})$  and  $r_{\mathcal{M}}(\mathbf{J}_{\text{MS}}, \mathbf{I}_{\text{MS}})$  are computed exactly.

##### 4.1. The Electric-Field Integral Equation

Instead of solving (59), we can equivalently solve (49) by setting

$$\begin{aligned} \mathbf{E}^{\mathcal{I}}(\mathbf{x}) &= \frac{j}{\epsilon\omega} \int_{S'} [k^2 \mathbf{J}_{\text{MS}}(\mathbf{x}') G(\mathbf{x}, \mathbf{x}') + \nabla' \cdot \mathbf{J}_{\text{MS}}(\mathbf{x}') \nabla G(\mathbf{x}, \mathbf{x}')] dS' \\ &\quad - \frac{1}{4} (\mathbf{n}(\mathbf{x}) \times \mathbf{I}_{\text{MS}}(\mathbf{x})) \delta_{\text{slot}}(\mathbf{x}) + \frac{1}{4\pi} \int_0^L \mathbf{I}_{\text{MS}}(s') \times \int_0^{2\pi} \nabla' G(\mathbf{x}, \mathbf{x}') d\phi' ds' + Z_s \mathbf{J}_{\text{MS}}(\mathbf{x}), \end{aligned} \quad (61)$$

where  $\delta_{\text{slot}}$  is defined such that

$$b_{\mathcal{E}}((\mathbf{n} \times \mathbf{I}_{\text{MS}}) \delta_{\text{slot}}, \boldsymbol{\Lambda}_i) = \int_S \boldsymbol{\Lambda}_i \cdot (\mathbf{n} \times \mathbf{I}_{\text{MS}}) \delta_{\text{slot}} dS = \int_0^L \boldsymbol{\Lambda}_i \cdot (\mathbf{n} \times \mathbf{I}_{\text{MS}}) ds. \quad (62)$$

Therefore, the manufactured source term for the EFIE is incorporated through the incident electric field, precluding the need for a dedicated manufactured source term.

##### 4.1.1. Manufactured Green's Function

As is done in [42, 44, 45], we manufacture the Green's function, using the form

$$G_{\text{MS}}(\mathbf{x}, \mathbf{x}') = G_q(\mathbf{x}, \mathbf{x}') = G_0 \left( 1 - \frac{R^2}{R_m^2} \right)^q, \quad (63)$$

where  $G_0 = 1 \text{ m}^{-1}$ ,  $q \in \mathbb{N}$ , and  $R_m = \max_{\mathbf{x}, \mathbf{x}' \in S} R$  is the maximum possible distance between two points on the domain. This form permits integrals of the Green's function and its derivatives to be computed exactly, avoiding contamination from numerical-integration error in convergence studies.

##### 4.2. The Slot Equation

Inserting (56) and (58) into (60) yields

$$a_{\mathcal{M},\mathcal{E}}(\mathbf{J}_h, \boldsymbol{\Lambda}_i^m) + a_{\mathcal{M},\mathcal{M}}(\mathbf{I}_h, \boldsymbol{\Lambda}_i^m) = a_{\mathcal{M},\mathcal{E}}(\mathbf{J}_{\text{MS}}, \boldsymbol{\Lambda}_i^m) + a_{\mathcal{M},\mathcal{M}}(\mathbf{I}_{\text{MS}}, \boldsymbol{\Lambda}_i^m). \quad (64)$$

As an alternative to solving (64), we can solve (50) by choosing  $\mathbf{I}_{\text{MS}}$ , such that, for a given  $\mathbf{J}_{\text{MS}}$ ,

$$a_{\mathcal{M},\mathcal{E}}(\mathbf{J}_{\text{MS}}, \boldsymbol{\Lambda}_i^m) + a_{\mathcal{M},\mathcal{M}}(\mathbf{I}_{\text{MS}}, \boldsymbol{\Lambda}_i^m) = 0. \quad (65)$$

As a result, the slot equation does not require a manufactured source term.

#### 4.2.1. Solution for Magnetic Current from a Known Electric Current

For a known  $\mathbf{J}$ , as is the case with  $\mathbf{J}_{\text{MS}}$ ,  $\mathbf{I}_m(s) = I_m(s)\mathbf{s}$  can be computed by solving (42). Projecting (42) at the inlet and outlet of the slot onto  $\mathbf{s}$  yields

$$r^-(s) = -J_s^-(s) + \frac{j\omega\epsilon}{2wL(k^2 - \beta_x^2)} \sum_{p=1}^{\infty} \beta_{y_p} \int_0^L \sin\left(\frac{p\pi s}{L}\right) \sin\left(\frac{p\pi s'}{L}\right) \times \\ \left([I_m^+(s') - I_m^-(s')] \tan(\beta_{y_p} d/2) + [I_m^+(s') + I_m^-(s')] \cot(\beta_{y_p} d/2)\right) ds' = 0, \quad (66)$$

$$r^+(s) = J_s^+(s) + \frac{j\omega\epsilon}{2wL(k^2 - \beta_x^2)} \sum_{p=1}^{\infty} \beta_{y_p} \int_0^L \sin\left(\frac{p\pi s}{L}\right) \sin\left(\frac{p\pi s'}{L}\right) \times \\ \left([I_m^-(s') - I_m^+(s')] \tan(\beta_{y_p} d/2) + [I_m^+(s') + I_m^-(s')] \cot(\beta_{y_p} d/2)\right) ds' = 0, \quad (67)$$

where  $J_s = (\mathbf{J} \times \mathbf{n}) \cdot \mathbf{s}$ . Adding (66) and (67) yields

$$J_s^+(s) - J_s^-(s) + \frac{j\omega\epsilon}{wL(k^2 - \beta_x^2)} \sum_{p=1}^{\infty} \beta_{y_p} \int_0^L \sin\left(\frac{p\pi s}{L}\right) \sin\left(\frac{p\pi s'}{L}\right) [I_m^+(s') + I_m^-(s')] \cot(\beta_{y_p} d/2) ds' = 0. \quad (68)$$

Subtracting (66) from (67) yields

$$J_s^-(s) + J_s^+(s) + \frac{j\omega\epsilon}{wL(k^2 - \beta_x^2)} \sum_{p=1}^{\infty} \beta_{y_p} \int_0^L \sin\left(\frac{p\pi s}{L}\right) \sin\left(\frac{p\pi s'}{L}\right) [I_m^-(s') - I_m^+(s')] \tan(\beta_{y_p} d/2) ds' = 0. \quad (69)$$

We express  $J_s$  and  $I_m$  as Fourier sine series

$$J_s(s) = \sum_{q=1}^{\infty} J_{s_q} \sin\left(\frac{q\pi s}{L}\right), \quad I_m(s) = \sum_{q=1}^{\infty} I_{m_q} \sin\left(\frac{q\pi s}{L}\right), \quad (70)$$

where

$$J_{s_q} = \frac{2}{L} \int_0^L J_s(s) \sin\left(\frac{q\pi s}{L}\right) ds. \quad (71)$$

To obtain the coefficients for  $I_m$  (70), we insert (70) into (68) and (69) and account for orthogonality (37):

$$I_{m_q}^- = \frac{jw(k^2 - \beta_x^2)}{\beta_{y_q} \omega \epsilon} \left( [J_{s_q}^+ - J_{s_q}^-] \tan(\beta_{y_q} d/2) + [J_{s_q}^- + J_{s_q}^+] \cot(\beta_{y_q} d/2) \right), \quad (72)$$

$$I_{m_q}^+ = \frac{jw(k^2 - \beta_x^2)}{\beta_{y_q} \omega \epsilon} \left( [J_{s_q}^+ - J_{s_q}^-] \tan(\beta_{y_q} d/2) - [J_{s_q}^- + J_{s_q}^+] \cot(\beta_{y_q} d/2) \right). \quad (73)$$

With (72) and (73), (70) provides the expression for  $I_m(s)$ .

#### 4.3. Solution-Discretization Error

In the absence of numerical-integration error, the only contribution to the discretization error is the solution-discretization error. Solving for  $\mathbf{J}^h$  and  $\mathbf{I}^h$  enables us to compute the discretization errors

$$\mathbf{e}_{\mathbf{J}} = \mathbf{J}^h - \mathbf{J}_n, \quad (74)$$

$$\mathbf{e}_{\mathbf{I}} = \mathbf{I}^h - \mathbf{I}_s, \quad (75)$$

where  $J_{n_j}$  denotes the component of  $\mathbf{J}_{\text{MS}}$  flowing from  $T_j^+$  to  $T_j^-$  and  $I_{s_j}$  denotes the component of  $\mathbf{I}_{\text{MS}}$  flowing along  $\mathbf{s}$  at position  $s_j$ . The norms of (74) and (75) have the properties  $\|\mathbf{e}_{\mathbf{J}}\| \leq C_{\mathbf{J}} h^{p_{\mathbf{J}}}$  and  $\|\mathbf{e}_{\mathbf{I}}\| \leq C_{\mathbf{I}} h^{p_{\mathbf{I}}}$ , where  $C_{\mathbf{J}}$  and  $C_{\mathbf{I}}$  are functions of the solution derivatives,  $h$  is representative of the mesh size, and  $p_{\mathbf{J}}$  and  $p_{\mathbf{I}}$

are the orders of accuracy. By performing a mesh-convergence study of the norms of the discretization errors, we can assess whether the expected orders of accuracy are obtained. For  $\mathbf{\Lambda}_j(\mathbf{x})$  and  $\mathbf{\Lambda}_j^m(s)$ , the expectation is second-order accuracy ( $p_{\mathbf{J}} = p_{\mathbf{I}} = 2$ ).

The first term in  $a_{\mathcal{E},\mathcal{M}}(\mathbf{u}, \mathbf{v})$  (14) introduces a discontinuity on the surface where the wire is located, which is characterized by  $\delta_{\text{slot}}$ , as described in (62). For the manufactured solutions, this implication is additionally present in  $\mathbf{E}^{\mathcal{I}}$  (61). This discontinuity will contaminate the convergence studies used to assess the correctness of the implementation of the numerical methods, reducing the convergence rate from  $\mathcal{O}(h^2)$  to  $\mathcal{O}(h)$  [53, 54].

To mitigate the effects of the discontinuity on the convergence studies, we consider two complementary approaches: (1) removing the discontinuity and (2) decoupling the discretization errors  $\mathbf{e}_{\mathbf{J}}$  (74) and  $\mathbf{e}_{\mathbf{I}}$  (75).

#### 4.3.1. Discontinuity Removal

To remove the discontinuity, we first separate the two terms in  $a_{\mathcal{E},\mathcal{M}}(\mathbf{u}, \mathbf{v})$ :

$$a_{\mathcal{E},\mathcal{M}}(\mathbf{u}, \mathbf{v}) = a_{\mathcal{E},\mathcal{M}_1}(\mathbf{u}, \mathbf{v}) + a_{\mathcal{E},\mathcal{M}_2}(\mathbf{u}, \mathbf{v}),$$

where

$$\begin{aligned} a_{\mathcal{E},\mathcal{M}_1}(\mathbf{u}, \mathbf{v}) &= -\frac{1}{4} \int_0^L \bar{\mathbf{v}} \cdot (\mathbf{n} \times \mathbf{u}) ds, \\ a_{\mathcal{E},\mathcal{M}_2}(\mathbf{u}, \mathbf{v}) &= \frac{1}{4\pi} \int_S \bar{\mathbf{v}}(\mathbf{x}) \cdot \int_0^L \mathbf{u}(s') \times \int_0^{2\pi} \nabla' G(\mathbf{x}, \mathbf{x}') d\phi' ds' dS, \end{aligned}$$

and  $a_{\mathcal{E},\mathcal{M}_1}(\mathbf{u}, \mathbf{v})$  is the term that introduces the discontinuity. We can write  $\mathbf{Z}$  (52) as

$$\mathbf{Z} = \begin{bmatrix} \mathbf{A} & (\mathbf{B}_1 + \mathbf{B}_2) \\ \mathbf{C} & \mathbf{D} \end{bmatrix}, \quad (76)$$

where  $B_{1i,j} = a_{\mathcal{E},\mathcal{M}_1}(\mathbf{\Lambda}_j^m, \mathbf{\Lambda}_i) \in \mathbb{R}$  and  $B_{2i,j} = a_{\mathcal{E},\mathcal{M}_2}(\mathbf{\Lambda}_j^m, \mathbf{\Lambda}_i) \in \mathbb{C}$ . Because  $a_{\mathcal{E},\mathcal{M}_1}(\mathbf{u}, \mathbf{v}) = -\frac{1}{4}a_{\mathcal{M},\mathcal{E}}(\bar{\mathbf{v}}, \bar{\mathbf{u}})$  and  $\mathbf{B}_1 = -\frac{1}{4}\mathbf{C}^T$ , (76) can be written as

$$\mathbf{Z} = \begin{bmatrix} \mathbf{A} & (-\frac{1}{4}\mathbf{C}^T + \mathbf{B}_2) \\ \mathbf{C} & \mathbf{D} \end{bmatrix}.$$

Taking the transpose of  $\mathbf{C}$ , dividing it by four, and adding it to  $\mathbf{B}$ , we can solve a modified problem, where  $\mathbf{Z}$  is modified to be

$$\mathbf{Z} = \begin{bmatrix} \mathbf{A} & \mathbf{B}_2 \\ \mathbf{C} & \mathbf{D} \end{bmatrix}, \quad (77)$$

and  $\mathbf{E}^{\mathcal{I}}$  (61) is modified to be

$$\begin{aligned} \mathbf{E}^{\mathcal{I}}(\mathbf{x}) &= \frac{j}{\epsilon\omega} \int_{S'} [k^2 \mathbf{J}_{\text{MS}}(\mathbf{x}') G(\mathbf{x}, \mathbf{x}') + \nabla' \cdot \mathbf{J}_{\text{MS}}(\mathbf{x}') \nabla G(\mathbf{x}, \mathbf{x}')] dS' \\ &\quad + \frac{1}{4\pi} \int_0^L \mathbf{I}_{\text{MS}}(s') \times \int_0^{2\pi} \nabla' G(\mathbf{x}, \mathbf{x}') d\phi' ds' + Z_s \mathbf{J}_{\text{MS}}(\mathbf{x}). \end{aligned} \quad (78)$$

With the modifications in (77) and (78), the discontinuity is removed. The correctness of the implementation of  $\mathbf{B}_1$  is assessed by its successful removal using  $\mathbf{C}$ , and the correctness of the implementation of  $\mathbf{C}$  is assessed through the aforementioned mesh-convergence study.

#### 4.3.2. Discretization Error Decoupling

To decouple the discretization errors  $\mathbf{e}_{\mathbf{J}}$  (74) and  $\mathbf{e}_{\mathbf{I}}$  (75), we reconsider the system of equations (51):

$$\begin{bmatrix} \mathbf{A} & \mathbf{B} \\ \mathbf{C} & \mathbf{D} \end{bmatrix} \begin{Bmatrix} \mathbf{J}^h \\ \mathbf{I}^h \end{Bmatrix} = \begin{Bmatrix} \mathbf{V}^{\mathcal{E}} \\ \mathbf{0} \end{Bmatrix}. \quad (79)$$

We can decouple the interaction of the discretization errors  $\mathbf{e}_J$  and  $\mathbf{e}_I$  by modifying (79) to be

$$\begin{bmatrix} \mathbf{A} & \mathbf{0} \\ \mathbf{0} & \mathbf{D} \end{bmatrix} \begin{Bmatrix} \mathbf{J}^h \\ \mathbf{I}^h \end{Bmatrix} = \begin{Bmatrix} \mathbf{V}^\mathcal{E} - \mathbf{B}\mathbf{I}_s \\ -\mathbf{C}\mathbf{J}_n \end{Bmatrix}, \quad (80)$$

where  $\mathbf{J}_n$  (74) and  $\mathbf{I}_s$  (75) are the exact solutions. In (80),  $\mathbf{e}_J$  and  $\mathbf{e}_I$  are independent of each other ( $\mathbf{e}_J \leftrightarrow \mathbf{e}_I$ ), but still depend on both  $\mathbf{J}_{\text{MS}}$  and  $\mathbf{I}_{\text{MS}}$ . By decoupling  $\mathbf{e}_J$  and  $\mathbf{e}_I$ , we expect their convergence rates to be  $\mathcal{O}(h)$  and  $\mathcal{O}(h^2)$ . Next, instead of fully decoupling the discretization errors, we can remove the influence of  $\mathbf{e}_I$  on  $\mathbf{e}_J$  while preserving the influence of  $\mathbf{e}_J$  on  $\mathbf{e}_I$  ( $\mathbf{e}_J \rightarrow \mathbf{e}_I$ ). The modification to (79) is

$$\begin{bmatrix} \mathbf{A} & \mathbf{0} \\ \mathbf{C} & \mathbf{D} \end{bmatrix} \begin{Bmatrix} \mathbf{J}^h \\ \mathbf{I}^h \end{Bmatrix} = \begin{Bmatrix} \mathbf{V}^\mathcal{E} - \mathbf{B}\mathbf{I}_s \\ \mathbf{0} \end{Bmatrix}. \quad (81)$$

Finally, we can remove the influence of  $\mathbf{e}_J$  on  $\mathbf{e}_I$  while preserving the influence of  $\mathbf{e}_I$  on  $\mathbf{e}_J$  ( $\mathbf{e}_J \leftarrow \mathbf{e}_I$ ). The modification to (79) is

$$\begin{bmatrix} \mathbf{A} & \mathbf{B} \\ \mathbf{0} & \mathbf{D} \end{bmatrix} \begin{Bmatrix} \mathbf{J}^h \\ \mathbf{I}^h \end{Bmatrix} = \begin{Bmatrix} \mathbf{V}^\mathcal{E} \\ -\mathbf{C}\mathbf{J}_n \end{Bmatrix}. \quad (82)$$

Assuming  $\mathbf{A}$  and  $\mathbf{D}$  are sufficiently conditioned, these approaches enable us to measure the discretization errors with various degrees of decoupling.

#### 4.4. Numerical-Integration Error

The integrals in (49) and (50) are evaluated numerically by integrating over each triangular or bar element using quadrature. Because these evaluations are generally approximations, it is important to measure the numerical-integration error without contamination from the solution-discretization error.

In [45], approaches are presented to isolate the numerical-integration error by canceling or eliminating the solution-discretization error. In this paper, we cancel the solution-discretization error and measure the numerical-integration error from

$$e_a = \mathcal{J}^H(\mathbf{Z}^q - \mathbf{Z})\mathcal{J}, \quad (83)$$

$$e_b = \mathcal{J}^H(\mathbf{V}^q - \mathbf{V}), \quad (84)$$

where

$$\mathcal{J} = \begin{Bmatrix} \mathbf{J}_n \\ \mathbf{I}_s \end{Bmatrix}.$$

Additionally,  $|e_a| \leq C_a h^{p_a}$  and  $|e_b| \leq C_b h^{p_b}$ , where  $C_a$  and  $C_b$  are functions of the integrand derivatives, and  $p_a$  and  $p_b$  depend on the quadrature accuracy. Unlike the solution-discretization error, the numerical-integration error is not contaminated by the discontinuity. Therefore, we use  $\mathbf{Z}$  (52) and  $\mathbf{E}^\mathcal{I}$  (61) without applying the modifications presented in Section 4.3.

## 5. Numerical Examples

In this section, we demonstrate the approaches described in Section 4 by isolating and measuring the solution-discretization error (Section 4.3) and the numerical-integration error (Section 4.4).

### 5.1. Domain and Coordinate Systems

In general, MMS allows considerable freedom for selecting the solution, geometry, parameters, and boundary conditions for the manufactured problem. However, sufficiently smooth solutions are required to permit detection of the correct convergence rates, and the interior and exterior surfaces of the scatterer are required to be polyhedra in order to be exactly represented by planar elements. The presence of the slot places additional constraints on the behavior of the solution in the vicinity of the slot. Furthermore, while geometries and solutions of arbitrary complexity may be used with MMS, additional complexity will generally incur additional computational expense. Therefore, we seek geometries and solutions that are simple, yet nontrivial.

For this work, we consider the scatterer geometry shown in Figure 2. The exterior surface is a cube, and the surface bounding the interior cavity is a triangular prism. The interior and exterior field domains are connected by a rectangularly prismatic slot. The slot is modeled by two wires, one at each opening. The dimensions of the scatterer are shown in Figure 3, where  $L^{\text{ext}} = 1$  m, and

$$L^{\text{int}} = \frac{2}{3}L^{\text{ext}}, \quad L = \frac{L^{\text{ext}}}{3}, \quad w = \frac{L^{\text{ext}}}{50}, \quad a^{\text{int}} = \frac{L^{\text{ext}}}{6}, \quad c^{\text{int}} = \frac{L^{\text{ext}}}{6}, \quad a^{\text{slot}} = \frac{L^{\text{ext}}}{3}, \quad z_0 = \frac{L^{\text{ext}}}{2}.$$

When undertaking code-verification activities, it is beneficial to consider a suite of similar cases with slightly different parameters, which aids in bug detection while minimizing the number of domains that must be meshed. For this problem, we consider two manufactured Green's functions (63):  $G_1$  and  $G_2$ , as well as three depths:  $d_1 = L^{\text{ext}}/5$ ,  $d_2 = L^{\text{ext}}/10$ , and  $d_3 = L^{\text{ext}}/20$ . For each of the three depths, an example discretization is shown in Figure 2 with  $n_t = 2240$  total triangles for the exterior and interior surfaces and four bar elements for each of the two wires. For the medium that surrounds the exterior of the scatterer and occupies the cavity interior, we set the permeability and permittivity of the surrounding medium to those of free space:  $\mu = \mu_0$  and  $\epsilon = \epsilon_0$ , assuming zero electrical conductivity ( $\sigma = 0$ ), and we set the wavenumber to  $k = 2\pi \text{ m}^{-1}$ . We set the electrical conductivity of the scatterer to that of aluminum. For the medium that occupies the slot interior, we set  $\mu = \mu_0$ ,  $\epsilon' = \epsilon_0$ , and  $\sigma = 5 \text{ S/m}$ . For the series in (45) and (46), we retain the first 150 terms.

To manufacture the surface current, we employ coordinate systems that wrap around the lateral surfaces of the exterior and interior domains [44]. We use  $\boldsymbol{\xi}_\theta$ , for the cube and triangular prism. For this coordinate system,  $\eta = y$  and  $\xi$  is perpendicular to  $y$ , wrapping counterclockwise (per the right-hand rule) around  $y$  along the surfaces for which  $\mathbf{n} \cdot \mathbf{e}_y = 0$ . For the cube,  $\eta \in [0, 1]L^{\text{ext}}$ , and  $\xi \in [0, 4]L^{\text{ext}}$ , beginning at  $x = 0$  and  $z = L^{\text{ext}}$ . For the triangular prism,  $\eta \in [a^{\text{int}}, b^{\text{int}}]$ , and  $\xi \in \xi_0 + [0, 3]L^{\text{int}}$ , where  $\xi_0 = 3(L^{\text{ext}} - L^{\text{int}})/2$ , beginning at  $x = x_0$  and  $z = z_0$ . For both the cube and the triangular prism, the wires are aligned with  $\xi_w = 3L^{\text{ext}}/2$  for  $\eta \in [a^{\text{slot}}, b^{\text{slot}}]$ . For the cube, we additionally use  $\boldsymbol{\xi}_\phi$ , for which  $\eta = x$  and  $\xi$  is perpendicular to  $x$ , wrapping counterclockwise around  $x$  along the surfaces for which  $\mathbf{n} \cdot \mathbf{e}_x = 0$ . Additionally,  $\eta \in [0, 1]L^{\text{ext}}$ , and  $\xi \in [0, 4]L^{\text{ext}}$ , beginning at  $y = L^{\text{ext}}$  and  $z = 0$ .

### 5.2. Manufactured Surface Current

We manufacture surface current densities for the cube and triangular prism using the aforementioned coordinate systems. For the cube,

$$\mathbf{J}_{\text{MS}}(\mathbf{x}) = J_{\xi_\theta}(\boldsymbol{\xi}_\theta)\mathbf{e}_{\xi_\theta} + J_{\xi_\phi}(\boldsymbol{\xi}_\phi)\mathbf{e}_{\xi_\phi}. \quad (85)$$

For the triangular prism,

$$\mathbf{J}_{\text{MS}}(\mathbf{x}) = J_{\xi_\theta}(\boldsymbol{\xi}_\theta)\mathbf{e}_{\xi_\theta}. \quad (86)$$

In (85) and (86),  $\mathbf{e}_{\xi_\theta} = (\partial\mathbf{x}/\partial\xi)_\theta$  and  $\mathbf{e}_{\xi_\phi} = (\partial\mathbf{x}/\partial\xi)_\phi$  in the  $\mathbf{x}$ -coordinate system. Additionally,

$$J_{\xi_\theta}(\boldsymbol{\xi}) = J_0 f_{\xi_\theta}(\xi) g_{\eta_\theta}(\eta), \quad (87)$$

$$J_{\xi_\phi}(\boldsymbol{\xi}) = J_0 f_{\xi_\phi}(\xi) g_{\eta_\phi}(\eta), \quad (88)$$

where  $J_0 = 1 \text{ A/m}$ .

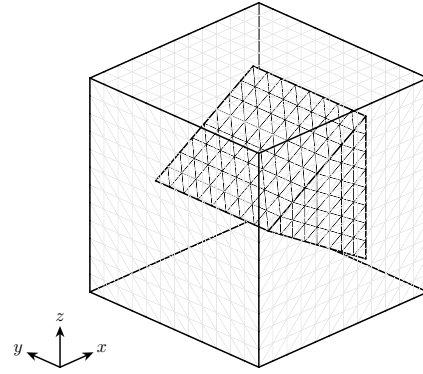
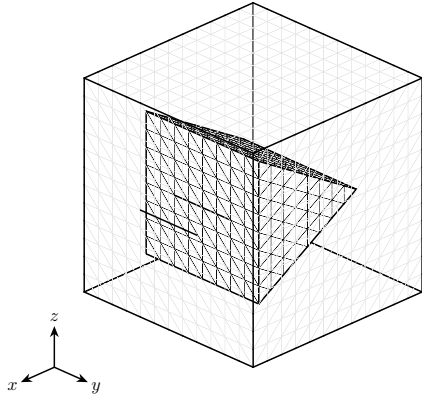
For  $f_\xi(\xi)$  and  $g_\eta(\eta)$ , we opt for nontrivial functions that are at least of class  $C^2$  with minimal oscillations, such that finer meshes are not required for mesh-convergence studies. For  $f_\xi(\xi)$ , we use periodic functions with a single period over the domain:

$$f_{\xi_\theta}(\xi) = \sin(\gamma(\xi - \bar{\xi}_1)),$$

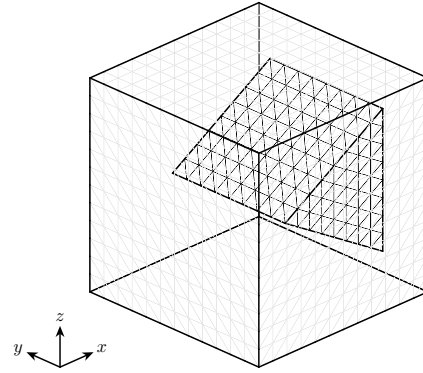
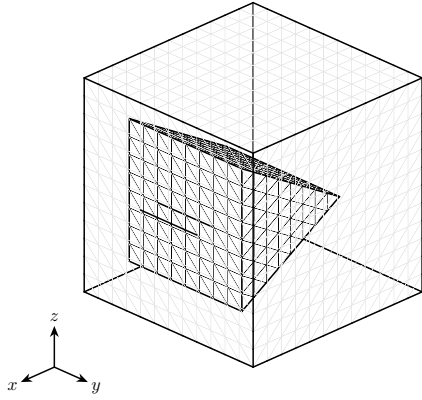
$$f_{\xi_\phi}(\xi) = \sin(\gamma(\xi - \bar{\xi}_2)).$$

For the cube,  $\gamma = \pi/(2L^{\text{ext}})$ ,  $\bar{\xi}_1 = 0$ , and  $\bar{\xi}_2 = L^{\text{ext}}/2$ ; for the triangular prism,  $\gamma = 2\pi/(3L^{\text{int}})$  and  $\bar{\xi}_1 = 5L^{\text{ext}}/4$ . For  $g_{\eta_\phi}(\eta)$ , the choice of

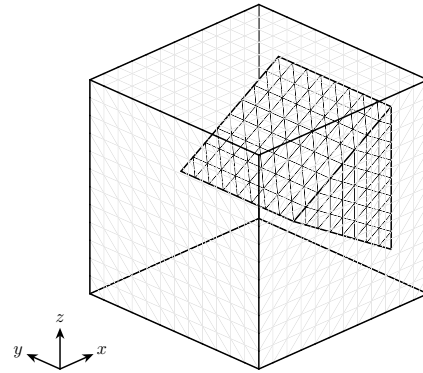
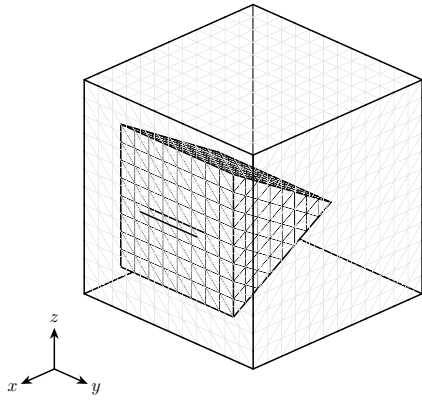
$$g_{\eta_\phi}(\eta) = \sin^3\left(\frac{\pi\eta}{L^{\text{ext}}}\right)$$



(a)  $d = d_1 = L^{\text{ext}}/5$



(b)  $d = d_2 = L^{\text{ext}}/10$



(c)  $d = d_3 = L^{\text{ext}}/20$

Figure 2: Meshed domain with  $n_t = 2240$  for 3 depths.

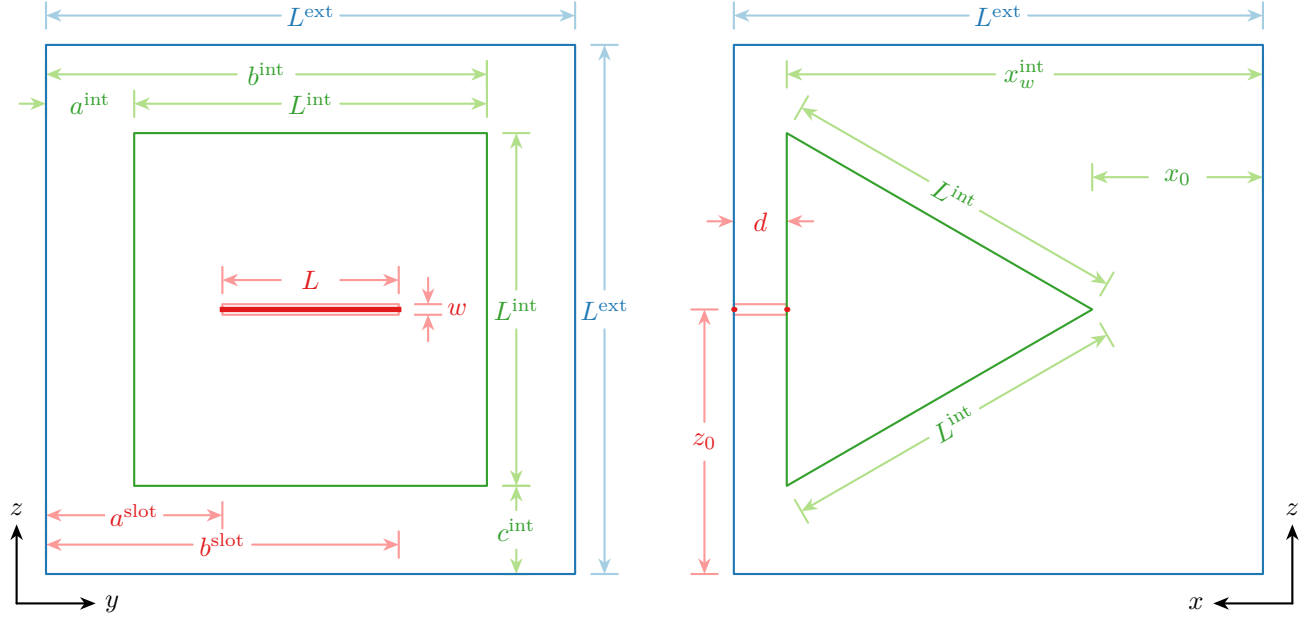


Figure 3: Dimensions of the domain.

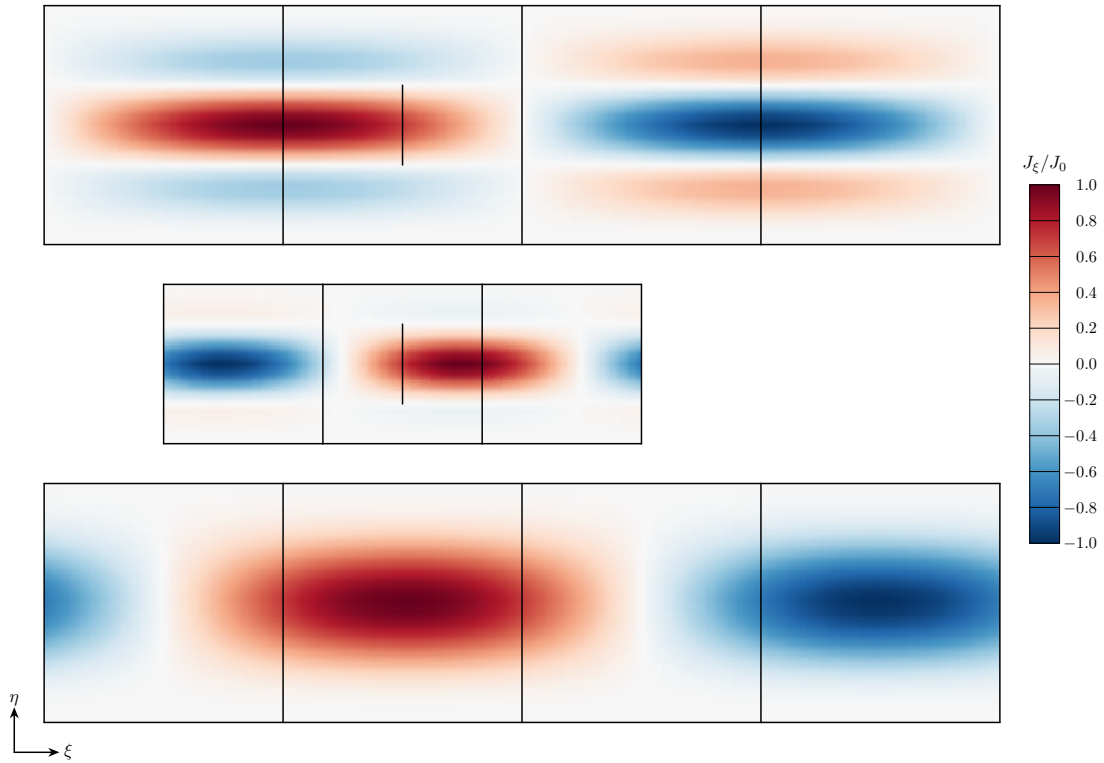


Figure 4: Manufactured surface current density  $\mathbf{J}_{MS}$ :  $J_{\xi_\theta}$  (87) for the cube (top) and triangular prism (middle), and  $J_{\xi_\phi}$  (88) for the cube (bottom).



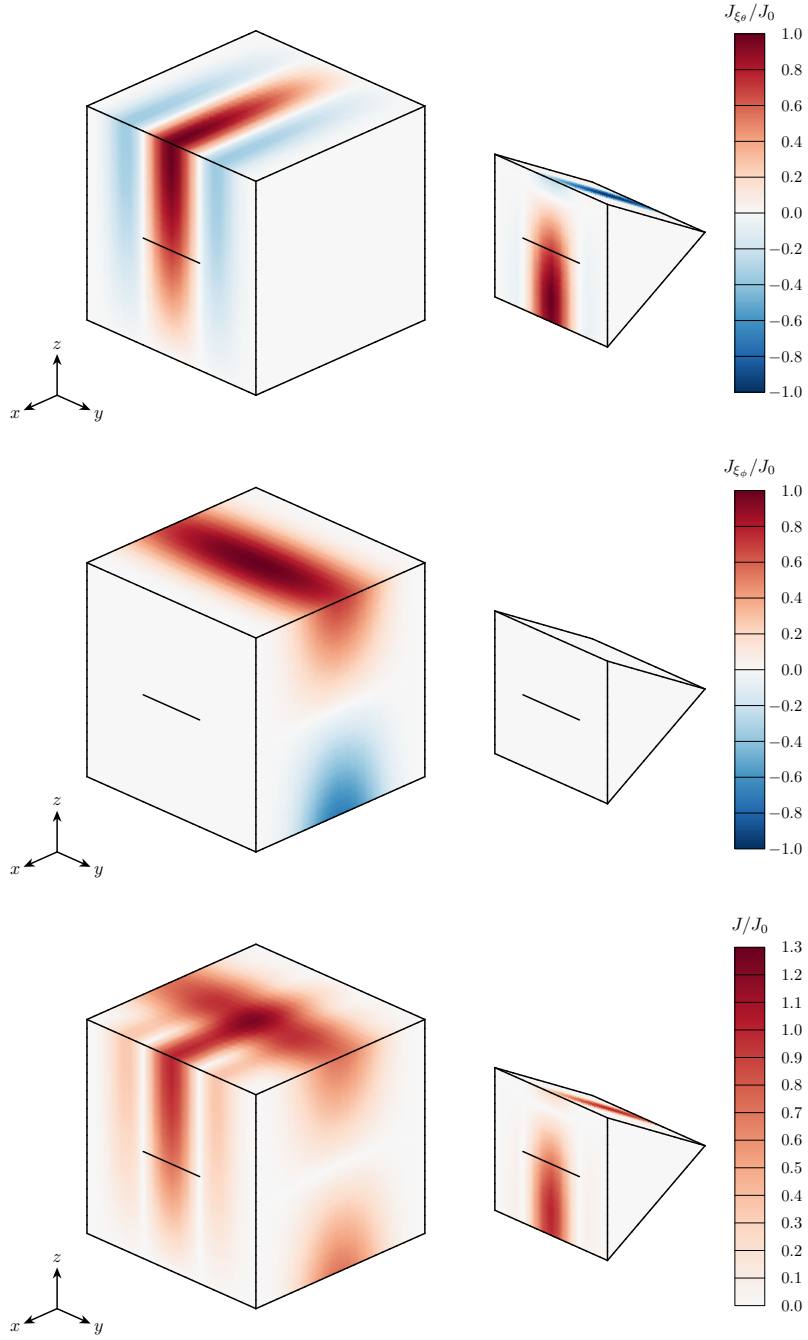


Figure 5: Manufactured surface current density  $\mathbf{J}_{\text{MS}}$ :  $J_{\xi_\theta}$  (87) (top),  $J_{\xi_\phi}$  (88) (middle), and  $J = |\mathbf{J}_{\text{MS}}|$  (85) and (86) (bottom).

results in  $g_{\eta_\theta}(\eta)$  and its first and second derivatives being zero at  $\eta = \{0, L^{\text{ext}}\}$ , such that it is of class  $C^2$  and is therefore suitable. Similarly,  $g_{\eta_\theta}(\eta)$  is of class  $C^2$  if  $g_{\eta_\theta}(\eta)$  and its first and second derivatives are zero at  $\eta = \{0, L^{\text{ext}}\} = \{a^{\text{ext}}, b^{\text{ext}}\}$  for the cube and  $\eta = \{a^{\text{int}}, b^{\text{int}}\}$  for the triangular prism. Additionally, from (70),  $g_{\eta_\theta}(\eta)$  must be zero at  $s = \{0, L\}$  ( $\eta = \{a^{\text{slot}}, b^{\text{slot}}\}$ ). Therefore, we choose

$$g_{\eta_\theta}(\eta) = \sum_{q=1}^3 C_q \sin\left(q' \pi \frac{\eta - a}{b - a}\right), \quad (89)$$

where  $q' = 2q - 1$ , to minimize oscillations. In (89), for the cube,  $a = a^{\text{ext}} = 0$  and  $b = b^{\text{ext}} = L^{\text{ext}}$ ; for the triangular prism,  $a = a^{\text{int}}$  and  $b = b^{\text{int}}$ . For the geometry described in Section 5.1,  $C^{\text{ext}} = \{1/4, -1/2, 1/4\}$  and  $C^{\text{int}} = \{1/2, -3/8, 1/8\}$ . In Figures 4 and 5, (87) is plotted for the cube and triangular prism, and (88) is plotted for the cube.

### 5.3. Magnetic Current

Next, instead of arbitrarily manufacturing  $\mathbf{I}_{\text{MS}}$ , we choose  $\mathbf{I}_{\text{MS}}(s) = I_m(s)\mathbf{s}$  to satisfy (65), given our choice of  $\mathbf{J}_{\text{MS}}$ .  $I_m(s)$  takes the form of (70), where, in (72) and (73),  $J_s(s)$  in (71) is

$$J_s(s) = J_0 f_{\xi_\theta}(\xi_w) g_{\eta_\theta}(\eta), \quad (90)$$

where  $s = \eta - a^{\text{slot}}$ . However, it is necessary to approximate  $I_m$  by truncating the infinite series. We note that, for the geometry and choices of  $J_s$  we consider,  $J_{s_q}$  in (70) is zero for even values of  $q$ ; therefore, our approximation for  $I_m$  (70) takes the form

$$I_{m_Q}(s) = \sum_{q=1}^Q I_{m_{q'}} \sin\left(\frac{q' \pi s}{L}\right), \quad (91)$$

where  $q' = 2q - 1$ .

For  $d \in \{d_1, d_2, d_3\}$ , Figure 6 shows the real and imaginary components of  $I_{m_Q}$ , normalized by  $I_0 = f_{\xi_\theta}(\xi_w)L^{\text{ext}}/d$  V for  $Q = 66$  in (91). To determine how well (91) satisfies (66) and (67), we insert (91) into (66) and (67), which yields

$$\begin{aligned} r_Q^-(s) &= -J_s^-(s) + \frac{j\omega\epsilon}{4w(k^2 - \beta_x^2)} \sum_{q=1}^Q \beta_{y_{q'}} \sin\left(\frac{q' \pi s}{L}\right) ([I_{m_{q'}}^+ - I_{m_{q'}}^-] \tan(\beta_{y_{q'}} d/2) + [I_{m_{q'}}^+ + I_{m_{q'}}^-] \cot(\beta_{y_{q'}} d/2)) \\ &= -J_s^-(s) + J_{s_Q}^-(s) \\ &= e_{J_Q}^-(s), \end{aligned} \quad (92)$$

$$\begin{aligned} r_Q^+(s) &= J_s^+(s) + \frac{j\omega\epsilon}{4w(k^2 - \beta_x^2)} \sum_{q=1}^Q \beta_{y_{q'}} \sin\left(\frac{q' \pi s}{L}\right) ([I_{m_{q'}}^- - I_{m_{q'}}^+] \tan(\beta_{y_{q'}} d/2) + [I_{m_{q'}}^+ + I_{m_{q'}}^-] \cot(\beta_{y_{q'}} d/2)) \\ &= J_s^+(s) - J_{s_Q}^+(s) \\ &= -e_{J_Q}^+(s), \end{aligned} \quad (93)$$

where

$$J_{s_Q}(s) = \sum_{q=1}^Q J_{s_{q'}} \sin\left(\frac{q' \pi s}{L}\right)$$

and

$$e_{J_Q}(s) = J_{s_Q}(s) - J_s(s).$$

Figure 7 shows the convergence of the coefficients  $J_{s_{q'}}$  and  $I_{m_{q'}}$  with respect to  $q$ , which are  $\mathcal{O}(q^{-3})$  and  $\mathcal{O}(q^{-4})$ , respectively, as derived in Appendix A.1 and Appendix A.2. Figure 8 shows the convergence of (92) and (93) with respect to  $Q$  by measuring

$$\|e_{J_Q}(s)\|_\infty = \max_{s \in [0, L]} |e_{J_Q}(s)|, \quad (94)$$

which, as derived in Appendix A.1, is  $\mathcal{O}(Q^{-2})$ .

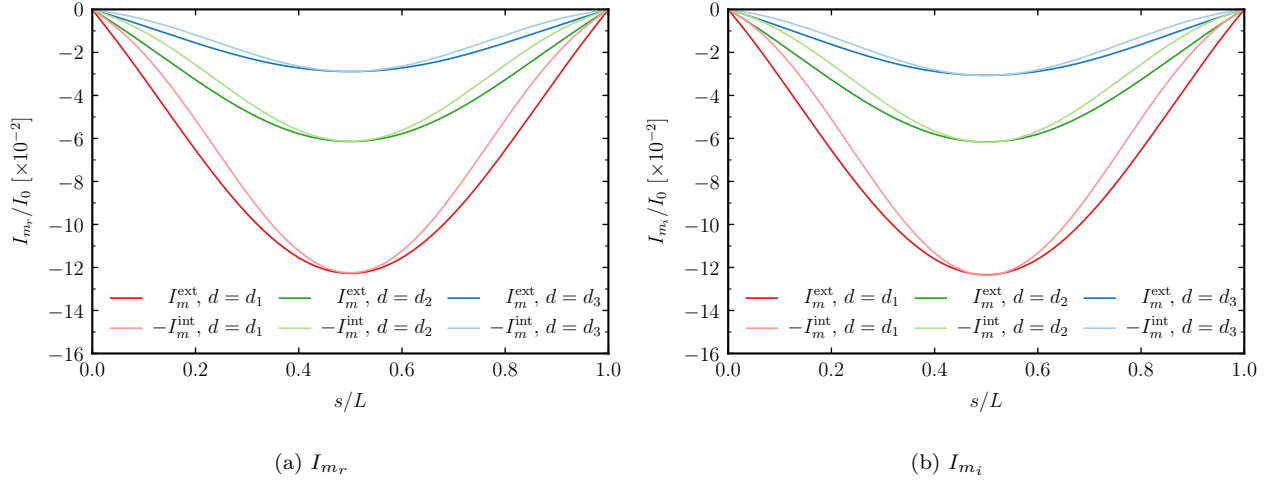


Figure 6: Real and imaginary components of  $I_{m_Q} = I_{m_r} + jI_{m_i}$  for 3 depths for  $Q = 66$  in (91).

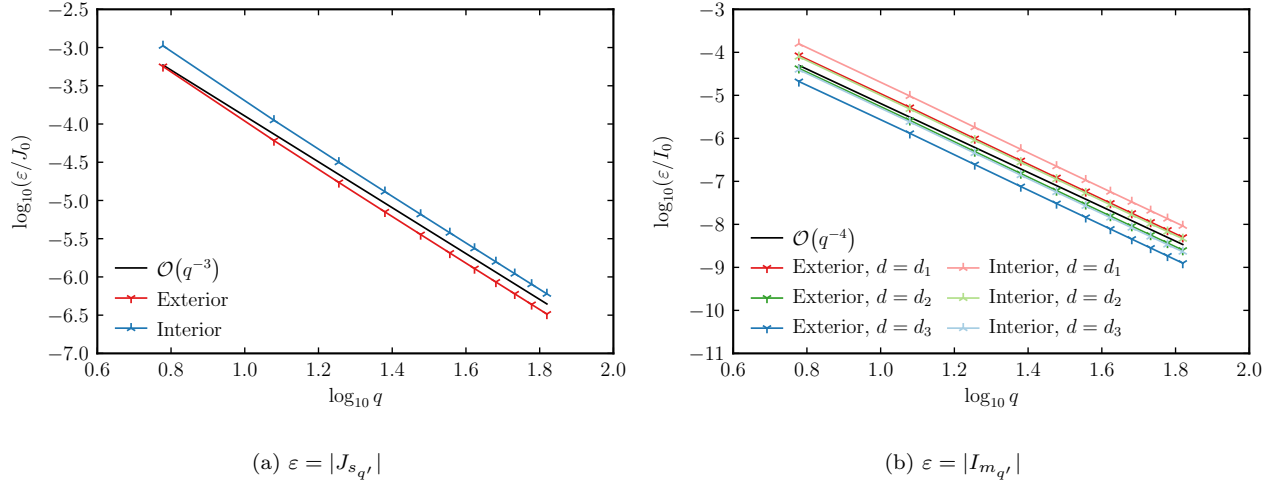


Figure 7: Sine series coefficient convergence.

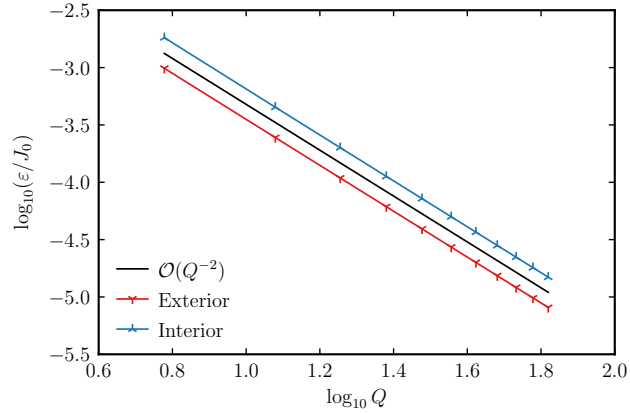
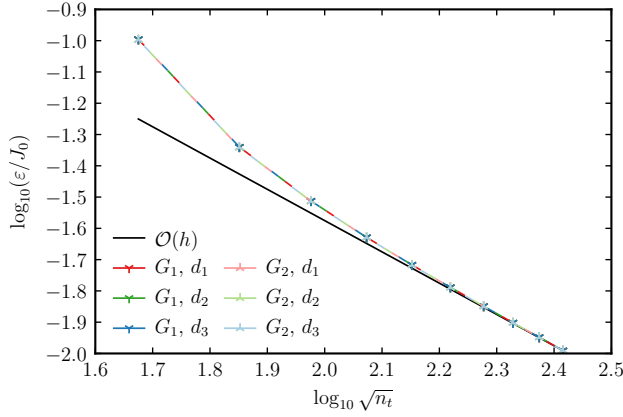
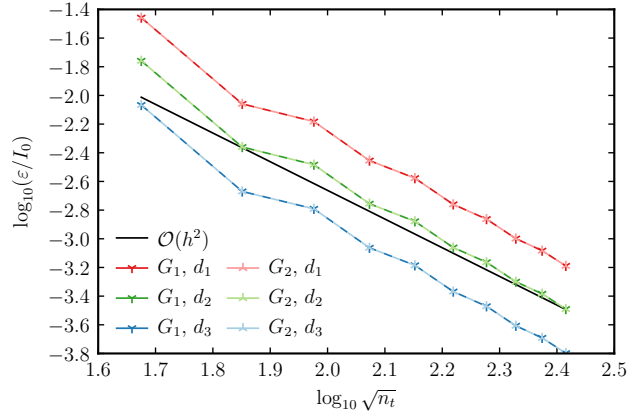


Figure 8: Slot equation series truncation error:  $\varepsilon = \|e_{J_Q}(s)\|_{\infty}$  (94).

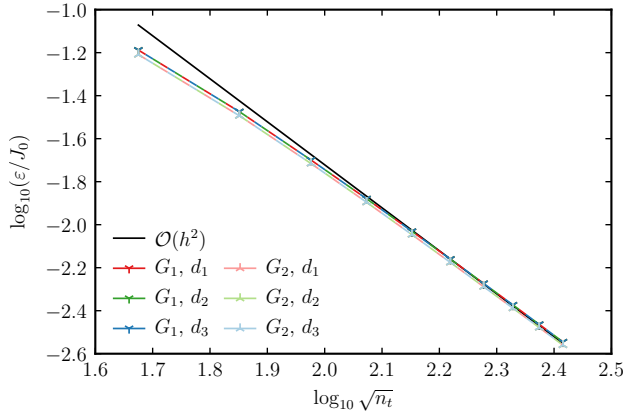


(a)  $\mathbf{e} = \mathbf{e}_J$  (74),  $\mathbf{e}_J \leftrightarrow \mathbf{e}_I$  (79)

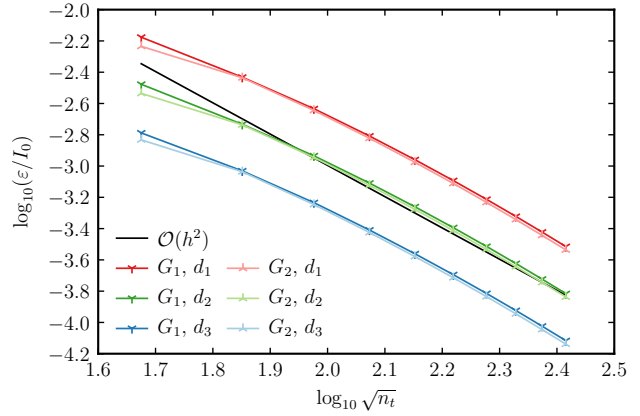


(b)  $\mathbf{e} = \mathbf{e}_I$  (75),  $\mathbf{e}_J \leftrightarrow \mathbf{e}_I$  (79)

Figure 9: Solution-discretization error:  $\varepsilon = \|\mathbf{e}\|_\infty$  with the discontinuity present.



(a)  $\mathbf{e} = \mathbf{e}_J$  (74)



(b)  $\mathbf{e} = \mathbf{e}_I$  (75)

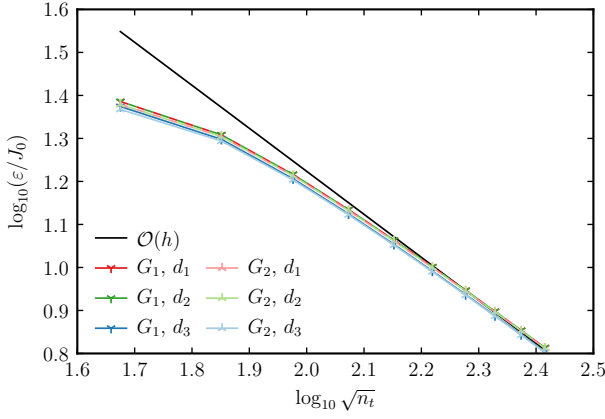
Figure 10: Solution-discretization error:  $\varepsilon = \|\mathbf{e}\|_\infty$  with the discontinuity removed.

#### 5.4. Solution-Discretization Error

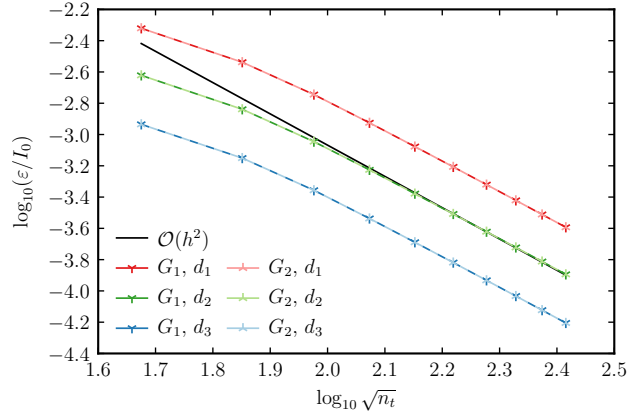
To isolate and measure the solution-discretization error, we proceed with the assessments described in Section 4.3, and we compute the integrals on both sides of (49) and (50) exactly.

The solution-discretization error arises from the basis-function approximation to the solution (47) and (48), as well as the truncation (91) of the sine series representation of  $I_m$  (70). The convergence rate of the basis functions is expected to be  $\mathcal{O}(h^2)$ . From Appendix A.2, the convergence rate of  $\|e_{I_Q}(s)\|_\infty$  (A.6) is expected to be  $\mathcal{O}(Q^{-3})$ . Therefore, to measure the convergence of the solution-discretization error, it is sufficient to refine the mesh and series at the same rate. Specifically, we set  $n_t = 140Q^2/9$ .

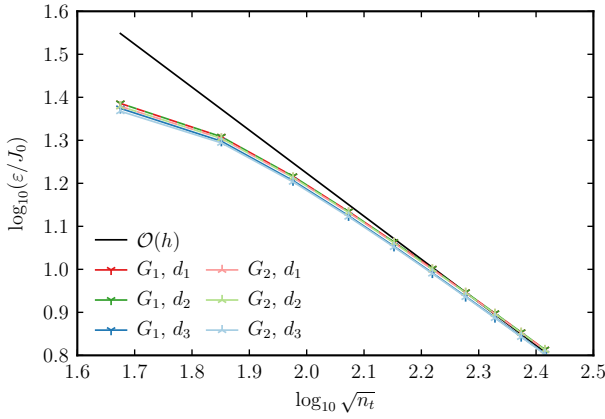
Additionally, the linear system is solved using a matrix-ready generalized minimum residual (GMRES) method [55]. Although Krylov-subspace methods are less frequently employed for dense matrices, GMRES is used here to allow parallelism to be extracted through distributed matrix-vector products. 200 basis vectors are used for all cases, which results in the ratio of the  $L^2$ -norm of the residual to the  $L^2$ -norm of the right-hand side being at most  $10^{-13}$ . Since the condition numbers of the matrices are estimated to be  $\mathcal{O}(10^7)$ , this tolerance is expected to yield a relative error of no more than  $\mathcal{O}(10^{-6})$  in the solution of the linear system. Therefore, we expect negligible contamination from iteration error.



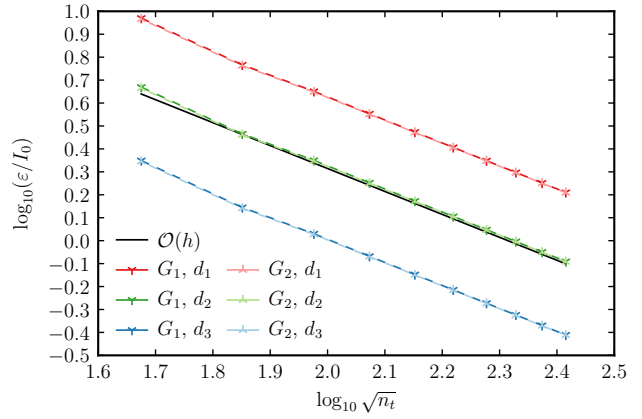
(a)  $\mathbf{e} = \mathbf{e}_J$  (74),  $\mathbf{e}_J \leftrightarrow \mathbf{e}_I$  (80)



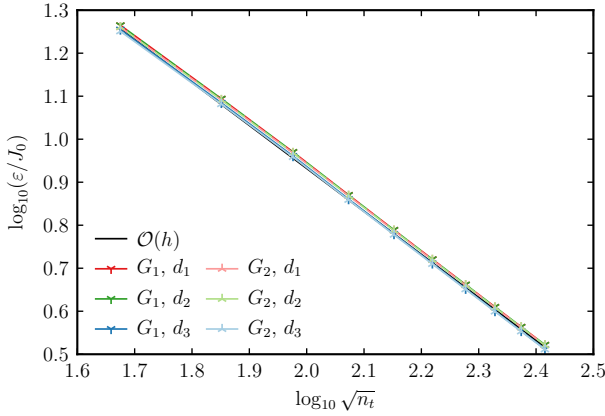
(b)  $\mathbf{e} = \mathbf{e}_I$  (75),  $\mathbf{e}_J \leftrightarrow \mathbf{e}_I$  (80)



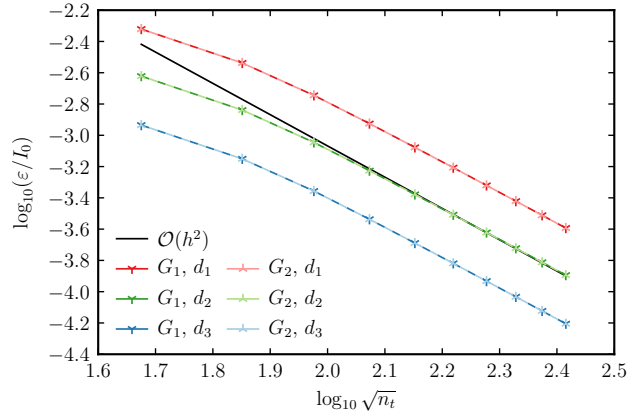
(c)  $\mathbf{e} = \mathbf{e}_J$  (74),  $\mathbf{e}_J \rightarrow \mathbf{e}_I$  (81)



(d)  $\mathbf{e} = \mathbf{e}_I$  (75),  $\mathbf{e}_J \rightarrow \mathbf{e}_I$  (81)



(e)  $\mathbf{e} = \mathbf{e}_J$  (74),  $\mathbf{e}_J \leftarrow \mathbf{e}_I$  (82)



(f)  $\mathbf{e} = \mathbf{e}_I$  (75),  $\mathbf{e}_J \leftarrow \mathbf{e}_I$  (82)

Figure 11: Solution-discretization error:  $\varepsilon = \|\mathbf{e}\|_\infty$  with the discontinuity present for different discretization error interactions.

Maximum integrand degree	Number of triangle points	Number of bar points	Convergence rate
1	1	1	$\mathcal{O}(h^2)$
2	3	—	$\mathcal{O}(h^4)$
3	4	2	$\mathcal{O}(h^4)$
4	6	—	$\mathcal{O}(h^6)$
5	7	3	$\mathcal{O}(h^6)$

Table 1: Polynomial quadrature rule properties.

In this subsection, we show the  $L^\infty$ -norm of the discretization errors (74) and (75):  $\|\mathbf{e}_J\|_\infty$  and  $\|\mathbf{e}_I\|_\infty$ , which arise from only the solution-discretization error. The error norms are shown for  $G_{\text{MS}} \in \{G_1, G_2\}$  (63) and  $d \in \{d_1, d_2, d_3\}$ .

Figure 9 shows the convergence rates when the discontinuity described in Section 4.3 is present. The convergence rate for  $\|\mathbf{e}_I\|_\infty$  is  $\mathcal{O}(h^2)$ , whereas the convergence rate for  $\|\mathbf{e}_J\|_\infty$  is  $\mathcal{O}(h)$ , each as expected.

Figure 10 shows the convergence rates when the discontinuity is removed, as described in Section 4.3.1. Using this approach, the convergence rates for  $\|\mathbf{e}_J\|_\infty$  and  $\|\mathbf{e}_I\|_\infty$  are both  $\mathcal{O}(h^2)$ , as expected.

Figure 11 shows the convergence rates using different approaches to decouple the discretization errors, as described in Section 4.3.2. Figures 11a and 11b show that, by decoupling  $\mathbf{e}_J$  and  $\mathbf{e}_I$  ( $\mathbf{e}_J \leftrightarrow \mathbf{e}_I$ ),  $\|\mathbf{e}_J\|_\infty$  is  $\mathcal{O}(h)$  in Figure 11a and  $\|\mathbf{e}_I\|_\infty$  is  $\mathcal{O}(h^2)$  in Figure 11b, both as expected. Figures 11c and 11d show that, by removing the influence of  $\mathbf{e}_I$  on  $\mathbf{e}_J$  but preserving the influence of  $\mathbf{e}_J$  on  $\mathbf{e}_I$  ( $\mathbf{e}_J \rightarrow \mathbf{e}_I$ ),  $\|\mathbf{e}_J\|_\infty$  is  $\mathcal{O}(h)$  in Figure 11c and  $\|\mathbf{e}_I\|_\infty$  is  $\mathcal{O}(h)$  in Figure 11d. Finally, Figures 11e and 11f show that, by removing the influence of  $\mathbf{e}_J$  on  $\mathbf{e}_I$  but preserving the influence of  $\mathbf{e}_I$  on  $\mathbf{e}_J$  ( $\mathbf{e}_J \leftarrow \mathbf{e}_I$ ),  $\|\mathbf{e}_J\|_\infty$  is  $\mathcal{O}(h)$  in Figure 11e and  $\|\mathbf{e}_I\|_\infty$  is  $\mathcal{O}(h^2)$  in Figure 11f.

### 5.5. Numerical-Integration Error

The numerical integration in (49) and (50) is performed using two-dimensional polynomial quadrature rules for triangles and one-dimensional polynomial quadrature rules for bars. Table 1 lists the maximum polynomial degree of the integrand that can be integrated exactly by optimal rules for various amounts of quadrature points in two dimensions [56, 57] and one dimension [58, Chap. 5], as well as the convergence rates of the errors for inexact integrations of nonsingular integrands.

When integrating the left-hand sides of (49) and (50), we note that, for  $G_1$ , four quadrature points integrate exactly for triangular elements and one point integrates exactly for bar elements. For  $G_2$ , seven quadrature points integrate exactly for triangular elements and two points integrate exactly for bar elements.

When integrating the right-hand side of (49), we note that the terms in  $b_{\mathcal{E}}(\mathbf{E}^T, \mathbf{\Lambda}_i)$ , excluding  $b_{\mathcal{E}}(Z_s \mathbf{J}_{\text{MS}}, \mathbf{\Lambda}_i)$  (61) and  $b_{\mathcal{E}}((\mathbf{n} \times \mathbf{I}_{\text{MS}}) \delta_{\text{slot}}, \mathbf{\Lambda}_i)$ , can be integrated exactly for triangular elements using four points for  $G_1$  and seven points for  $G_2$ . The contributions to  $b_{\mathcal{E}}(\mathbf{E}^T, \mathbf{\Lambda}_i)$  from  $b_{\mathcal{E}}(Z_s \mathbf{J}_{\text{MS}}, \mathbf{\Lambda}_i)$  (61) and  $b_{\mathcal{E}}((\mathbf{n} \times \mathbf{I}_{\text{MS}}) \delta_{\text{slot}}, \mathbf{\Lambda}_i)$  are computed analytically.

To isolate and measure the numerical-integration error, we perform the assessments described in Section 4.4. As explained in Appendix A.3, the integral of the truncation error associated with  $I_{m_Q}$  is  $\mathcal{O}(Q^{-4})$ . Therefore, if  $Q \sim 1/h$ , where  $1/h \sim \sqrt{n_t}$ , as in Section 5.4, the convergence rate will be limited to  $\mathcal{O}(h^4)$ .

Figures 12 and 13 show the numerical-integration errors  $e_a$  (83) and  $e_b$  (84) for  $G_2$  and  $d_1$ . We consider different amounts of triangle quadrature points for each simulation. The simulation entries in the legends take the form  $n_q^t \times n_q^s$ , where  $n_q^t$  and  $n_q^s$  respectively denote the amounts of quadrature points used to evaluate the test and source integrals. The numerical-integration error is nondimensionalized by the constant  $\varepsilon_0 = 1 \text{ A}\cdot\text{V}$ . The number of bar quadrature points is chosen to match the convergence rates of the triangle quadrature points. The entries in the left column of the legends are for reference convergence rates. The simulation entries in a given row are expected to have the same convergence rates as the reference rate, as listed in Table 1.

For these assessments, we consider  $Q = 1$  in Figures 12a and 13a and  $Q = \sqrt{n_t/140}$  in Figures 12b and 13b. In Figures 12a, 12b and 13a, the quadrature points converge at the expected rates, whereas, in Figure 13b the convergence rates are limited to  $\mathcal{O}(h^4)$ , as expected, due to integral of the truncation

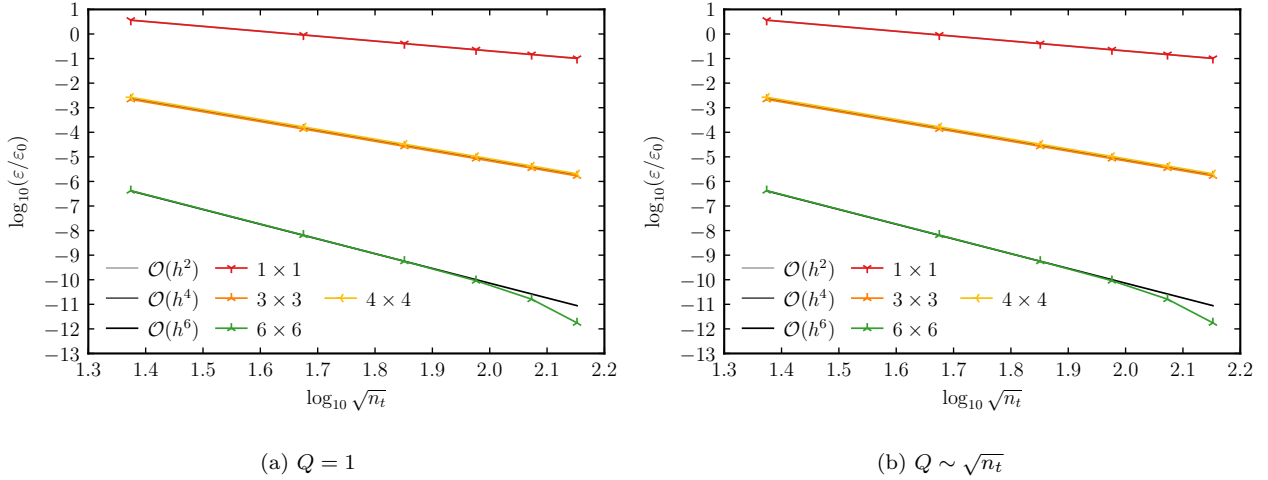


Figure 12: Numerical-integration error:  $\varepsilon = |e_a|$  (83) for  $G_2$  and  $d_1$  with different amounts of quadrature points.

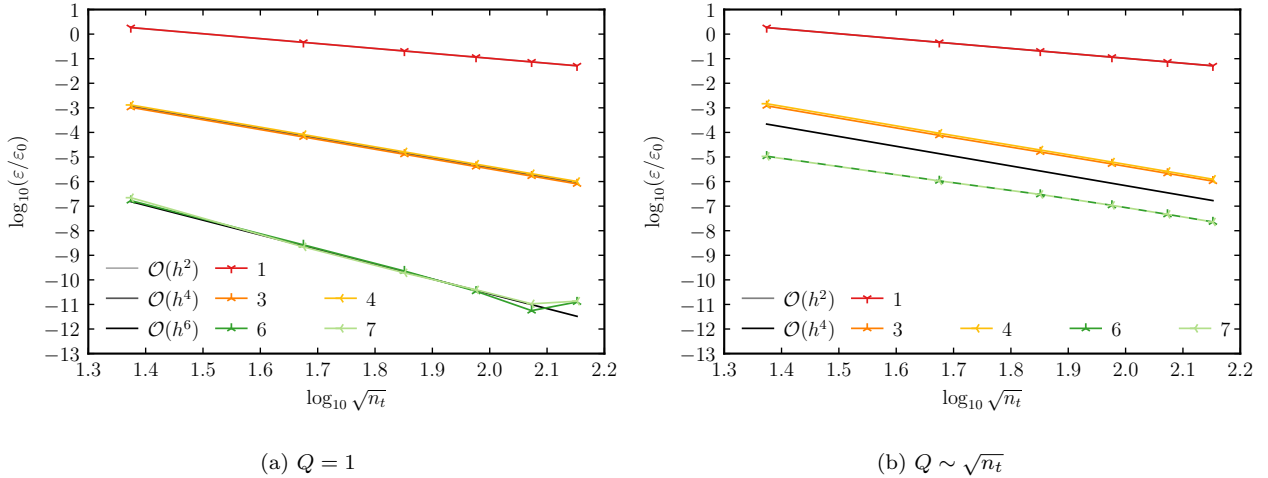


Figure 13: Numerical-integration error:  $\varepsilon = |e_b|$  (84) for  $G_2$  and  $d_1$  with different amounts of quadrature points.

error associated with  $I_{m_Q}$ . For the finest meshes and largest numbers of quadrature points considered, the round-off error arising from the double-precision calculations exceeds the numerical-integration error.

## 6. Conclusions

In this paper, we presented code-verification approaches to isolate and measure the solution-discretization error and numerical-integration error for an arbitrary-depth slot model that was coupled with the electric-field integral equation. We manufactured the surface current density, which yielded a source term that we incorporated as a manufactured incident field for the EFIE. Given the manufactured surface current, we obtained a sine series expression for the magnetic current that did not require a source term in the slot equation.

We isolated and measured the solution-discretization error by integrating exactly over the domain using a manufactured Green's function. To avoid contamination from the sine series truncation and the iterative

solver, we refined the sine series truncation with the mesh and we kept the error due to the iterative solver sufficiently low. On each surface, the interaction between the wire and the surface introduced a line discontinuity, which can contaminate convergence studies. We mitigated this problem by removing the discontinuity using other entries from the matrix that undergo code verification. We alternatively kept the discontinuity and varied the interaction between the discretization errors to demonstrate the implications. To isolate the numerical-integration error, we removed the solution-discretization error and demonstrated the implications of the sine series truncation error on convergence. For both approaches, we performed convergence studies for a variety of configurations for which we achieved the expected orders of accuracy.

## Acknowledgments

This article has been authored by employees of National Technology & Engineering Solutions of Sandia, LLC under Contract No. DE-NA0003525 with the U.S. Department of Energy (DOE). The employees own all right, title, and interest in and to the article and are solely responsible for its contents. The United States Government retains and the publisher, by accepting the article for publication, acknowledges that the United States Government retains a non-exclusive, paid-up, irrevocable, world-wide license to publish or reproduce the published form of this article or allow others to do so, for United States Government purposes. The DOE will provide public access to these results of federally sponsored research in accordance with the DOE Public Access Plan <https://www.energy.gov/downloads/doe-public-access-plan>.

## Appendix A. Sine Series Convergence

### A.1. $J_s(s)$

For our manufactured  $J_s(s)$  (90),  $J_{s_{q'}}$  (71) is

$$J_{s_{q'}}^- = \frac{\delta_{1q'}}{2} - \frac{108\sqrt{3}q'}{\pi(81q'^4 - 234q'^2 + 25)}, \quad J_{s_{q'}}^+ = -\frac{48\sqrt{2}(4q'^3 - 17q')}{\pi(64q'^6 - 560q'^4 + 1036q'^2 - 225)}, \quad (\text{A.1})$$

where  $q' = 2q - 1$ . Letting

$$e_{J_Q}(s) = J_{s_Q}(s) - J_s(s) = -\sum_{q=Q+1}^{\infty} J_{s_{q'}} \sin\left(\frac{q'\pi s}{L}\right)$$

and

$$\|e_{J_Q}(s)\|_{\infty} = \max_{s \in [0, L]} |e_{J_Q}(s)|, \quad (\text{A.2})$$

we note that  $|\sin(q'\pi s/L)| \leq 1$ , such that, in (A.2),

$$|e_{J_Q}(s)| \leq \sum_{q=Q+1}^{\infty} |J_{s_{q'}}|. \quad (\text{A.3})$$

From (A.1), for sufficiently large  $q'$ ,

$$|J_{s_{q'}}| \leq C_{J_{q'}} q'^{-3}. \quad (\text{A.4})$$

Therefore,  $|J_{s_{q'}}|$  is  $\mathcal{O}(q^{-3})$ , which is shown in Figure 7a. In (A.3),

$$\sum_{q=Q+1}^{\infty} |J_{s_{q'}}| \leq C_{J_{\infty}} \sum_{q=Q+1}^{\infty} q'^{-3} \approx C_{J_{\infty}} \int_{Q+1}^{\infty} q'^{-3} dq' = \frac{C_{J_{\infty}}}{2} (Q+1)^{-2},$$

where  $C_{J_{\infty}}$  is an upper bound for  $C_{J_{q'}}$ . Consequently,  $\|e_{J_Q}(s)\|_{\infty}$  is  $\mathcal{O}(Q^{-2})$ , which is shown in Figure 8.



### A.2. $I_m(s)$

As shown in (72) and (73),  $I_{m_{q'}}$  is related to  $q'$  through a linear combination of  $[J_{s_{q'}}^+ - J_{s_{q'}}^-] \tan(\beta_{y_{q'}} d/2)/\beta_{y_{q'}}$  and  $[J_{s_{q'}}^- + J_{s_{q'}}^+] \cot(\beta_{y_{q'}} d/2)/\beta_{y_{q'}}$ . Noting that, from (41) and (31), for large values of  $q'$ ,

$$\beta_{y_{q'}} \approx j \frac{q' \pi}{L},$$

and

$$\begin{aligned} \frac{\tan(\beta_{y_{q'}} d/2)}{\beta_{y_{q'}}} &\approx \frac{L \tanh(q' \pi d/(2L))}{q' \pi} \approx \frac{L}{q' \pi}, \\ \frac{\cot(\beta_{y_{q'}} d/2)}{\beta_{y_{q'}}} &\approx -\frac{L \coth(q' \pi d/(2L))}{q' \pi} \approx -\frac{L}{q' \pi}. \end{aligned}$$

such that both are  $\mathcal{O}(q^{-1})$ . From (A.4),  $[J_{s_{q'}}^+ - J_{s_{q'}}^-] \tan(\beta_{y_{q'}} d/2)/\beta_{y_{q'}}$  and  $[J_{s_{q'}}^- + J_{s_{q'}}^+] \cot(\beta_{y_{q'}} d/2)/\beta_{y_{q'}}$  are  $\mathcal{O}(q^{-4})$ . Consequently,  $I_{m_{q'}}$  is  $\mathcal{O}(q^{-4})$ :

$$|I_{m_{q'}}| \leq C_{I_{q'}} q'^{-4},$$

which is shown in Figure 7b. Let

$$e_{I_Q}(s) = I_{m_Q}(s) - I_m(s) = -\sum_{q=Q+1}^{\infty} I_{m_{q'}} \sin\left(\frac{q' \pi s}{L}\right) \quad (\text{A.5})$$

and

$$\|e_{I_Q}(s)\|_{\infty} = \max_{s \in [0, L]} |e_{I_Q}(s)|. \quad (\text{A.6})$$

In (A.6),

$$|e_{I_Q}(s)| \leq \sum_{q=Q+1}^{\infty} |I_{m_{q'}}|, \quad (\text{A.7})$$

and, in (A.7),

$$\sum_{q=Q+1}^{\infty} |I_{m_{q'}}| \leq C_{I_{\infty}} \sum_{q=Q+1}^{\infty} q'^{-4} \approx C_{I_{\infty}} \int_{Q+1}^{\infty} q'^{-4} dq' = \frac{C_{I_{\infty}}}{3} (Q+1)^{-3},$$

where  $C_{I_{\infty}}$  is an upper bound for  $C_{I_{q'}}$ . Therefore,  $\|e_{I_Q}(s)\|_{\infty}$  is  $\mathcal{O}(Q^{-3})$ .

### A.3. Integration of $I_m(s)$

When integrating  $I_{m_Q}$  over different meshes and increasing  $Q$  with  $n_t$ ,  $e_{I_Q}(s)$  (A.5) introduces an error. To derive the convergence rate of this error, we begin by considering the integral of the error:

$$\int_0^L e_{I_Q}(s) ds = -\sum_{q=Q+1}^{\infty} I_{m_{q'}} \int_0^L \sin\left(\frac{q' \pi s}{L}\right) ds = -\frac{2L}{\pi} \sum_{q=Q+1}^{\infty} \frac{I_{m_{q'}}}{q'},$$

which can be bounded by

$$\left| \int_0^L e_{I_Q}(s) ds \right| \leq \frac{2L}{\pi} \sum_{q=Q+1}^{\infty} \frac{|I_{m_{q'}}|}{q'} \leq \frac{2L}{\pi} \sum_{q=Q+1}^{\infty} C_{I_{q'}} q'^{-5} \approx C_{I_{\infty}} \int_{Q+1}^{\infty} q'^{-5} dq' = \frac{C_{I_{\infty}}}{4} (Q+1)^{-4}.$$

Therefore,  $|\int_0^L e_{I_Q}(s) ds|$  is  $\mathcal{O}(Q^{-4})$ . When assessing the convergence rate of the numerical integration, if  $Q \sim 1/h$ , where  $1/h \sim \sqrt{n_t}$ , and the integration error convergence is faster than  $\mathcal{O}(h^4)$ , the convergence rate will be limited to  $\mathcal{O}(h^4)$ , as shown in Figure 13b. While  $Q$  can be increased faster than  $h$ ,  $Q$  can instead be made constant to avoid this issue, as shown in Figure 13a.

## References

- [1] C. M. Butler, Y. Rahmat-Samii, R. Mittra, Electromagnetic penetration through apertures in conducting surfaces, *IEEE Transactions on Electromagnetic Compatibility* 20 (1978). doi:10.1109/TEMC.1978.303696.
- [2] C. A. Balanis, *Advanced Engineering Electromagnetics*, John Wiley & Sons, Inc., 2012.
- [3] L. Warne, K. Chen, Relation between equivalent antenna radius and transverse line dipole moments of a narrow slot aperture having depth, *IEEE Transactions on Electromagnetic Compatibility* 30 (3) (1988) 364–370. doi:10.1109/15.3316.
- [4] S. A. Schelkunoff, H. T. Friis, *Antennas: Theory and Practice*, John Wiley & Sons, Inc., 1952.
- [5] G. Cerri, R. D. Leo, V. M. Primiani, Theoretical and experimental evaluation of the electromagnetic radiation from apertures in shielded enclosure, *IEEE Transactions on Electromagnetic Compatibility* 34 (1992). doi:10.1109/15.179275.
- [6] R. P. Jedlicka, *Electromagnetic coupling into complex cavities through narrow slot apertures having depth and losses*, PhD dissertation, New Mexico State University (Dec. 1995).
- [7] M. P. Robinson, T. M. Benson, C. Christopoulos, J. F. Dawson, M. Ganley, A. Marvin, S. Porter, D. W. Thomas, Analytical formulation for the shielding effectiveness of enclosures with apertures, *IEEE Transactions on Electromagnetic Compatibility* 40 (1998). doi:10.1109/15.709422.
- [8] R. Araneo, G. Lovat, An efficient MoM formulation for the evaluation of the shielding effectiveness of rectangular enclosures with thin and thick apertures, *IEEE Transactions on Electromagnetic Compatibility* 50 (2008). doi:10.1109/TEMC.2008.919031.
- [9] D. A. Hill, *Electromagnetic Fields in Cavities: Deterministic and Statistical Theories*, Wiley-IEEE Press, 2009. doi:10.1002/9780470495056.
- [10] D. M. Pozar, *Microwave Engineering*, John Wiley & Sons, Inc., 2011.
- [11] S. Campione, L. K. Warne, W. L. Langston, R. A. Pfeiffer, N. Martin, J. T. Williams, R. K. Gutierrez, I. C. Reines, J. G. Huerta, V. Q. Dang, Penetration through slots in cylindrical cavities operating at fundamental cavity modes, *IEEE Transactions on Electromagnetic Compatibility* 62 (2020). doi:10.1109/TEMC.2020.2977600.
- [12] L. K. Warne, W. A. Johnson, B. F. Zinser, W. L. Langston, R. S. Coats, I. C. Reines, J. T. Williams, L. I. Basillio, K. C. Chen, *Narrow slot algorithm*, Sandia Report SAND2020-3979, Sandia National Laboratories (Apr. 2020). doi:10.2172/1615888.
- [13] M. Illescas, *Improved experimental validation of an electromagnetic subcell model for narrow slots with depth*, Master’s thesis, University of New Mexico (May 2023).
- [14] P. J. Roache, *Verification and Validation in Computational Science and Engineering*, Hermosa Publishers, 1998.
- [15] P. Knupp, K. Salari, *Verification of Computer Codes in Computational Science and Engineering*, Chapman & Hall/CRC, 2002. doi:10.1201/9781420035421.
- [16] W. L. Oberkampf, C. J. Roy, *Verification and Validation in Scientific Computing*, Cambridge University Press, 2010. doi:10.1017/cbo9780511760396.
- [17] P. J. Roache, Code verification by the method of manufactured solutions, *Journal of Fluids Engineering* 124 (1) (2001) 4–10. doi:10.1115/1.1436090.
- [18] C. J. Roy, C. C. Nelson, T. M. Smith, C. C. Ober, Verification of Euler/Navier–Stokes codes using the method of manufactured solutions, *International Journal for Numerical Methods in Fluids* 44 (6) (2004) 599–620. doi:10.1002/flid.660.

- [19] R. B. Bond, C. C. Ober, P. M. Knupp, S. W. Bova, Manufactured solution for computational fluid dynamics boundary condition verification, *AIAA Journal* 45 (9) (2007) 2224–2236. doi:[10.2514/1.28099](https://doi.org/10.2514/1.28099).
- [20] S. Veluri, C. Roy, E. Luke, Comprehensive code verification for an unstructured finite volume CFD code, in: 48th AIAA Aerospace Sciences Meeting including the New Horizons Forum and Aerospace Exposition, American Institute of Aeronautics and Astronautics, 2010. doi:[10.2514/6.2010-127](https://doi.org/10.2514/6.2010-127).
- [21] É. Chamberland, A. Fortin, M. Fortin, Comparison of the performance of some finite element discretizations for large deformation elasticity problems, *Computers & Structures* 88 (11) (2010) 664 – 673. doi:[10.1016/j.compstruc.2010.02.007](https://doi.org/10.1016/j.compstruc.2010.02.007).
- [22] A. Amar, N. Calvert, B. Kirk, Development and verification of the charring ablating thermal protection implicit system solver, in: 49th AIAA Aerospace Sciences Meeting including the New Horizons Forum and Aerospace Exposition, 2011. doi:[10.2514/6.2011-144](https://doi.org/10.2514/6.2011-144).
- [23] T. Oliver, K. Estacio-Hiroms, N. Malaya, G. Carey, Manufactured solutions for the Favre-averaged Navier–Stokes equations with eddy-viscosity turbulence models, in: 50th AIAA Aerospace Sciences Meeting including the New Horizons Forum and Aerospace Exposition, American Institute of Aeronautics and Astronautics, 2012. doi:[10.2514/6.2012-80](https://doi.org/10.2514/6.2012-80).
- [24] S. Étienne, A. Garon, D. Pelletier, Some manufactured solutions for verification of fluid–structure interaction codes, *Computers & Structures* 106–107 (2012) 56–67. doi:[10.1016/j.compstruc.2012.04.006](https://doi.org/10.1016/j.compstruc.2012.04.006).
- [25] A. Veeraragavan, J. Beri, R. J. Gollan, Use of the method of manufactured solutions for the verification of conjugate heat transfer solvers, *Journal of Computational Physics* 307 (2016) 308–320. doi:[10.1016/j.jcp.2015.12.004](https://doi.org/10.1016/j.jcp.2015.12.004).
- [26] L. Eça, C. M. Klaij, G. Vaz, M. Hoekstra, F. Pereira, On code verification of RANS solvers, *Journal of Computational Physics* 310 (2016) 418–439. doi:[10.1016/j.jcp.2016.01.002](https://doi.org/10.1016/j.jcp.2016.01.002).
- [27] A. Hennink, M. Tiberga, D. Lathouwers, A pressure-based solver for low-Mach number flow using a discontinuous Galerkin method, *Journal of Computational Physics* 425 (2022). doi:[10.1016/j.jcp.2020.109877](https://doi.org/10.1016/j.jcp.2020.109877).
- [28] B. A. Freno, B. R. Carnes, V. G. Weirs, Code-verification techniques for hypersonic reacting flows in thermochemical nonequilibrium, *Journal of Computational Physics* 425 (2021). doi:[10.1016/j.jcp.2020.109752](https://doi.org/10.1016/j.jcp.2020.109752).
- [29] B. A. Freno, B. R. Carnes, V. E. Brunini, N. R. Matula, Nonintrusive manufactured solutions for non-decomposing ablation in two dimensions, *Journal of Computational Physics* 463 (2022). doi:[10.1016/j.jcp.2022.111237](https://doi.org/10.1016/j.jcp.2022.111237).
- [30] M. Bukač, G. Fu, A. Seboldt, C. Trenchea, Time-adaptive partitioned method for fluid–structure interaction problems with thick structures, *Journal of Computational Physics* 473 (2023). doi:[10.1016/j.jcp.2022.111708](https://doi.org/10.1016/j.jcp.2022.111708).
- [31] F. Bukreev, S. Simonis, A. Kummerländer, J. Jeßberger, M. J. Krause, Consistent lattice Boltzmann methods for the volume averaged Navier–Stokes equations, *Journal of Computational Physics* 490 (2023). doi:[10.1016/j.jcp.2023.112301](https://doi.org/10.1016/j.jcp.2023.112301).
- [32] I. Fumagalli, M. Corti, N. Parolini, P. F. Antonietti, Polytopal discontinuous Galerkin discretization of brain multiphysics flow dynamics, *Journal of Computational Physics* 513 (2024). doi:[10.1016/j.jcp.2024.113115](https://doi.org/10.1016/j.jcp.2024.113115).
- [33] R. G. McClarren, R. B. Lowrie, Manufactured solutions for the  $p_1$  radiation-hydrodynamics equations, *Journal of Quantitative Spectroscopy and Radiative Transfer* 109 (15) (2008) 2590–2602. doi:[10.1016/j.jqsrt.2008.06.003](https://doi.org/10.1016/j.jqsrt.2008.06.003).

- [34] F. Riva, C. F. Beadle, P. Ricci, A methodology for the rigorous verification of particle-in-cell simulations, *Physics of Plasmas* 24 (2017). doi:10.1063/1.4977917.
- [35] A. Amor-Martin, L. E. Garcia-Castillo, J.-F. Lee, Study of accuracy of a non-conformal finite element domain decomposition method, *Journal of Computational Physics* 429 (2021). doi:10.1016/j.jcp.2020.109989.
- [36] P. Tranquilli, L. Ricketson, L. Chacón, A deterministic verification strategy for electrostatic particle-in-cell algorithms in arbitrary spatial dimensions using the method of manufactured solutions, *Journal of Computational Physics* 448 (2022). doi:10.1016/j.jcp.2021.110751.
- [37] A. M. Rueda-Ramírez, F. J. Hindenlang, J. Chan, G. J. Gassner, Entropy-stable Gauss collocation methods for ideal magneto-hydrodynamics, *Journal of Computational Physics* 475 (2023). doi:10.1016/j.jcp.2022.111851.
- [38] J. Rudi, M. Heldman, E. M. Constantinescu, Q. Tang, X.-Z. Tang, Scalable implicit solvers with dynamic mesh adaptation for a relativistic drift-kinetic Fokker–Planck–Boltzmann model, *Journal of Computational Physics* 507 (2024). doi:10.1016/j.jcp.2024.112954.
- [39] O. Issan, O. Koshkarov, F. D. Halpern, B. Kramer, G. L. Delzanno, Anti-symmetric and positivity preserving formulation of a spectral method for Vlasov–Poisson equations, *Journal of Computational Physics* 514 (2024). doi:10.1016/j.jcp.2024.113263.
- [40] R. G. Marchand, The method of manufactured solutions for the verification of computational electromagnetic codes, PhD dissertation, Stellenbosch University (Mar. 2013).
- [41] R. G. Marchand, D. B. Davidson, Verification of the method-of-moment codes using the method of manufactured solutions, *IEEE Transactions on Electromagnetic Compatibility* 56 (4) (2014) 835–843. doi:10.1109/TEMC.2014.2325826.
- [42] B. A. Freno, N. R. Matula, W. A. Johnson, Manufactured solutions for the method-of-moments implementation of the electric-field integral equation, *Journal of Computational Physics* 443 (2021). doi:10.1016/j.jcp.2021.110538.
- [43] B. A. Freno, N. R. Matula, J. I. Owen, W. A. Johnson, Code-verification techniques for the method-of-moments implementation of the electric-field integral equation, *Journal of Computational Physics* 451 (2022). doi:10.1016/j.jcp.2021.110891.
- [44] B. A. Freno, N. R. Matula, R. A. Pfeiffer, E. A. Dohme, J. D. Kotulski, Manufactured solutions for an electromagnetic slot model, *Journal of Computational Physics* 516 (2024). doi:10.1016/j.jcp.2024.113343.
- [45] B. A. Freno, N. R. Matula, Code-verification techniques for the method-of-moments implementation of the magnetic-field integral equation, *Journal of Computational Physics* 478 (2023). doi:10.1016/j.jcp.2023.111959.
- [46] B. A. Freno, N. R. Matula, Code-verification techniques for the method-of-moments implementation of the combined-field integral equation, *Journal of Computational Physics* 488 (2023). doi:10.1016/j.jcp.2023.112231.
- [47] L. Warne, K. Chen, Slot apertures having depth and losses described by local transmission line theory, *IEEE Transactions on Electromagnetic Compatibility* 32 (3) (1990) 185–196. doi:10.1109/15.57112.
- [48] L. Warne, K. Chen, A simple transmission line model for narrow slot apertures having depth and losses, *IEEE Transactions on Electromagnetic Compatibility* 34 (3) (1992) 173–182. doi:10.1109/15.155827.
- [49] L. K. Warne, Eddy current power dissipation at sharp corners: Rectangular conductor examples, *Electromagnetics* 15 (3) (1995) 273–290. doi:10.1080/02726349508908419.

- [50] W. A. Johnson, L. K. Warne, R. E. Jorgenson, J. D. Kotulski, H. G. Hudson, S. L. Stronach, Incorporation of slot subcell models into EIGER for treatment of high Q cavity coupling problems, Sandia Report SAND2002-2681J, Sandia National Laboratories (Jul. 2002).
- [51] S. Rao, D. Wilton, A. Glisson, Electromagnetic scattering by surfaces of arbitrary shape, *IEEE Transactions on Antennas and Propagation* 30 (3) (1982) 409–418. [doi:10.1109/TAP.1982.1142818](https://doi.org/10.1109/TAP.1982.1142818).
- [52] K. F. Warnick, *Numerical Analysis for Electromagnetic Integral Equations*, Artech House, 2008.
- [53] C. D’Angelo, Finite element approximation of elliptic problems with Dirac measure terms in weighted spaces: Applications to one- and three-dimensional coupled problems, *SIAM Journal on Numerical Analysis* 50 (1) (2012). [doi:10.1137/100813853](https://doi.org/10.1137/100813853).
- [54] H. Li, X. Wan, P. Yin, L. Zhao, Regularity and finite element approximation for two-dimensional elliptic equations with line Dirac sources, *Journal of Computational and Applied Mathematics* 393 (2021). [doi:10.1016/j.cam.2021.113518](https://doi.org/10.1016/j.cam.2021.113518).
- [55] Y. Saad, M. H. Schultz, GMRES: A generalized minimal residual algorithm for solving nonsymmetric linear systems, *SIAM Journal on Scientific and Statistical Computing* 7 (3) (1986). [doi:10.1137/0907058](https://doi.org/10.1137/0907058).
- [56] J. N. Lyness, D. Jespersen, Moderate degree symmetric quadrature rules for the triangle, *IMA Journal of Applied Mathematics* 15 (1) (1975) 19–32. [doi:10.1093/imamat/15.1.19](https://doi.org/10.1093/imamat/15.1.19).
- [57] D. A. Dunavant, High degree efficient symmetrical Gaussian quadrature rules for the triangle, *International Journal for Numerical Methods in Engineering* 21 (6) (1985) 1129–1148. [doi:10.1002/nme.1620210612](https://doi.org/10.1002/nme.1620210612).
- [58] D. Kahaner, C. Moler, S. Nash, *Numerical Methods and Software*, Prentice Hall, 1989.